Politecnico
di Torino

ScuDo
Scuola di Dottorato ~ Doctoral School
WHAT YOU ARE, TAKES YOU FAR

Doctoral Dissertation
Doctoral Program in Mechanical Engineering (36th Cycle)

A multiscale, statistical approach to model open-hole strength size effect in woven composites

Andrea Ferrarese

******

Supervisor
Prof. Davide Salvatore Paolino

Politecnico di Torino
2024

I hereby declare that, the contents and organisation of this dissertation constitute my own original work and does not compromise in any way the rights of third parties, including those relating to the security of personal data.

……………………………………

Andrea Ferrarese

Summary

The variation of strength of composite parts with size is referred to as the size effect, and it can be observed in the presence of notches such as circular open holes. In woven composites, when the characteristic size of the interlocking tows of fibers and the notches is comparable, the material heterogeneity and stress concentration interact, giving rise to a complex stress field. Existing analysis of open-hole strength however focuses on unidirectional composites and does not model this effect. This study proposes to investigate the size effect on circular open-hole strength of a woven twill composite using a novel experimental-numerical approach, capable of preserving the mesoscale material heterogeneity captured by full-field Digital Image Correlation (DIC) measurements, and to use this information as the basis for a statistical reliability method.

An innovative simplified mesoscale model was thus developed, which recaptures the heterogeneity of the woven material. The aim was to obtain a full stress field corresponding to the DIC-measured experimental strain field. First, the experimental strains were obtained via uniaxial tensile testing of open-hole specimens. Local material orientation was mapped in every individual specimen using a semi-automated image processing script, and applied to a shell model of each specimen. The mesoscopic elastic material properties of the material were identified with a data-driven FEMU optimization method, which minimized the difference between the experimental DIC strains, and the one predicted by the model itself. This model was able to replicate the effect of the woven pattern of the fabric in a computationally efficient way.

A probabilistic mesoscale method was then developed to model the size effect. A three-parameter Weibull-based statistical model was devised to model the probability of failure from the mesoscale FEM calculated stress distribution and the volume of the part. An equivalent stress formulation was used to capture the relevant failure modes, and its maximum value within the specimen volume was the random variable of the model. The parameters of the statistical model and of the equivalent stress were calibrated with an optimization process from experimental data.

The methodology was successfully applied to study the effect of specimen width and width-to-diameter ratio on the open-hole strength of a twill CFRP material. The elastic properties identified for the material at the mesoscale were analogous to that of a unidirectional composite. The calibrated model was subsequently used to analyze the stress concentration and localization induced by circular notches with various widths and width-to-diameter ratios. Thanks to the stress data, the macroscale-level behavior was interpreted as the combination of two opposing mesoscale-level effects, stress concentration and stress localization. An observable size effect was produced with varying specimen width, whereas the scaling of width to hole diameter ratio in the range considered did not. The statistical model was found to accurately describe the experimental observations, efficiently reproducing an inverse size effect: wider specimens lead to a lower probability of failure, regardless of hole size.

Contents

List of tables

List of figures

Chapter 1

Introduction

Size effect is the phenomenon of scaling of a material's mechanical property with structure dimensions. This effect can occur in the tensile strength of long-fiber-reinforced composite materials, where it typically decreases with increasing structure size [1]. In general, size effect is observed in brittle and quasi-brittle materials [2], of which high-modulus fiber composites are an example. In these materials, failure is governed by the presence of statistically distributed defects. Given two volumes of material at the same stress level, the larger one has a higher chance of containing a flaw critical enough to initiate the failure. In other words, the probability of encountering a failure-inducing defect depends on the volume of the material considered [3].

The tensile strength of hole-notched composites under tension is a classic example of size effect, often studied in the literature. A circular notch shape is usually selected, due to its relevance in fastening applications like bolted connections or riveting. Existing methods usually require either very extensive experimental campaigns to derive semi-empirical laws, or numerical models with complex damage models to predict the initiation of failure. Furthermore, almost invariably unidirectional fiber composites are considered. Woven fiber composites introduce further challenges to the study, as their heterogeneous structure at the mesoscale can interact with notches and generate stress fields that are non-trivial to model.

This work proposes to advance the knowledge of the open-hole size effect on tensile strength in twill weave composites with a statistical method that considers the mesoscale heterogeneity of these materials. The method, based on the Weibull weakest link principle, allows bypassing the definition of complex interacting failure models. A novel experimental-numerical approach to the study of woven composites provides the necessary mesoscale stress data.

This introductory chapter is structured as follows. Section 1.1 delineates the main problem through a review of existing literature. The subsequent three sections synthetically present one by one the main aspects underpinning the methodology developed in this thesis. Section 1.2 introduces briefly the Digital Image Correlation measurement technique, and then presents some applications relevant to this work. Section 1.3 gives an overview of the statistical modeling of composite strength after the Weibull strength theory. Section 1.4 discusses woven fabric composites and how they can be modeled. At the end of the chapter Section 1.5 states the objectives of this thesis, defines the various steps in the methodology, and lays out the organization of this work.

1.1 Open-hole size effect in composite materials

The problem of the open-hole size effect in composite materials has been investigated using a number of different approaches, which may be broadly classified as follows:

- Experimental campaigns [4,5], also paired with full-field strain field analysis [6–8];
- Semi-empirical methods [9–11], with empirical formulations based on observed failures that model the tensile strength of open-hole specimens. The most common criteria are the point stress and the average stress ones, developed by Whitney and Nuismer in 1974 [9,12], whose purpose is to predict the decrease in strength at specimen or component level. These criteria have been extended to different composites in various studies [13–16], or used to validate numerical studies [17].
- Finite element methods that address the complexity of the problem by incorporating different damage models, aiming to describe the interaction of failure modes (e.g., delamination, in-plane cracking) and validating numerical results with experimental ones [18–26]; advanced finite element methods have also been used [27–30];
- Hybrid methods that integrate experimental observation with numerical models, using Digital Image Correlation (DIC) for full-field measurement of the strain [31];

- Analytical methods that derive the exact stress field around the notch, using equilibrium and constitutive equations to predict the component failure [32].

In this work experiments and finite element modeling are used as the basis for a statistical approach.

Almost the entirety of the existing studies has focused on unidirectional [4–7,16,18–25,27–31] or biaxial [14,15] fiber composites. Analysis of fabric composites however presents additional challenges compared to unidirectional laminates, in that there is an interaction between the stress concentration and the heterogeneous structure of the woven lamina. Specifically, almost no studies consider twill fabric, one of the most commonly used in composite manufacturing. While there is literature on simulating twill composites with an open hole [33] and application of more conventional semi-empirical methods [13–15], there is a knowledge gap on the size effect in these composites considering their heterogeneous structure. This work will apply the developed methodology, well-suited to the study of woven composites, to a twill fabric CFRP.

The factors influencing size effect that are most commonly studied include the stacking sequence ([15,23,26,31]), laminate thickness [22,25]), also distinguishing between ply- and sublaminate-level scaling ([4,18,19]), hole diameter ([4,5,19–21,24]), and the type of reinforcement fibers ([14,15,26]). For this study, width and width-to-diameter ratio were selected.

1.2 Application of Digital Image Correlation to the study of composites

Digital Image Correlation (DIC) is a non-contact, image-based measurement method, used to measure the full shape, displacement, and deformation fields of an object. DIC has become increasingly popular in mechanical testing in the past 20 years, thanks to the availability of good quality digital cameras and ready-to-use commercial DIC software. At its core DIC uses an image matching algorithm correlating a small portion of a reference image, called a subset, and a displaced and/or deformed version in another. The motion and deformation fields are thus identified. The algorithm works by minimizing the difference in grey values between the subset in the reference and deformed image; for application to mechanical deformation measurement, DIC incorporates shape functions similar to those used in the finite element method, able to handle complex deformation and rotations [34]. For the image matching algorithm to function properly, the imaged object needs to have high-contrast, isotropic, non-repeating features—ideally a random texture, which has the highest information content. Usually, these textures resemble laser speckle patterns, and are applied by painting, so that they form a coating that deforms with the object.

When processing images from a single camera, DIC is able to measure displacement and deformations in-plane only, and is known as 2D DIC. Calibration for 2D DIC involves simply measuring the size in pixels in the recorded image of a feature with known dimensions. While having the upside of simplicity, 2D DIC is sensitive to any out-of-plane movements, including accidental shifts of the camera system. They will be registered as fictitious in-plane displacements, and will be very difficult to separate from the actual ones.

3D DIC overcomes these limitations by using a stereoscopic camera system, essentially combining photogrammetry and digital image correlation [35]. By recording simultaneously the same point with a second camera, a 3D displacement vector can be recovered from two 2-dimensional ones. A more complex calibration process is needed, to establish the coordinate transformation between the two camera systems and the external global reference system. This is normally done by imaging a grid of high-contrast points with known spacing.

DIC can be used to replace traditional contact strain measurements such as strain gauges or extensometers, with the definite advantages of being a non-contact and non-point measurement. The full-field capabilities of DIC are useful when characterizing heterogeneous materials, where high spatial resolution data is needed, and for identification of micromechanical material properties [36]. The study of stress concentration in composite materials, with their intrinsic heterogeneity and anisotropy, has also greatly benefited from full-field techniques like DIC; digital image correlation [37], but also electronic speckle pattern interferometry [38], and the grid method [6,7] have been used as well. Figure 1 shows an example of a heterogeneous longitudinal stress field in a notched uniaxial tension specimen made from woven composite, obtained with DIC. A common application of DIC measurements to this problem is for validating a finite element analysis, by comparing the measured strain field with the numerical results [18,23,27]. The DIC strain field can be used in tandem with a finite element model, such as to analyze the already discussed open-hole tensile problem in twill composite [33].

Another application of the full-field capability of DIC concerns the determination of material model parameters, using integrated experimental-numerical approaches [14,35,39–41]. These methods are typically a variant of the numerical scheme known as Finite Element Model-Updating. In these methods, a Finite Element Model (FEM) is solved iteratively. The strains outputted at every step are compared with the experimental ones using an appropriate objective function, formulated for the specific problem. An optimization algorithm then updates the values of the material model parameters to be identified, aiming to minimize the objective function. Upon reaching a predetermined convergence criterion, the resulting parameters are the calibrated material properties [22]. An approach of this type was used by [26] at proof-of-concept level with synthetic data to determine the material properties of composite constituents at the microscale level. A FEMU scheme was implemented in this work to obtain mesoscale material properties.

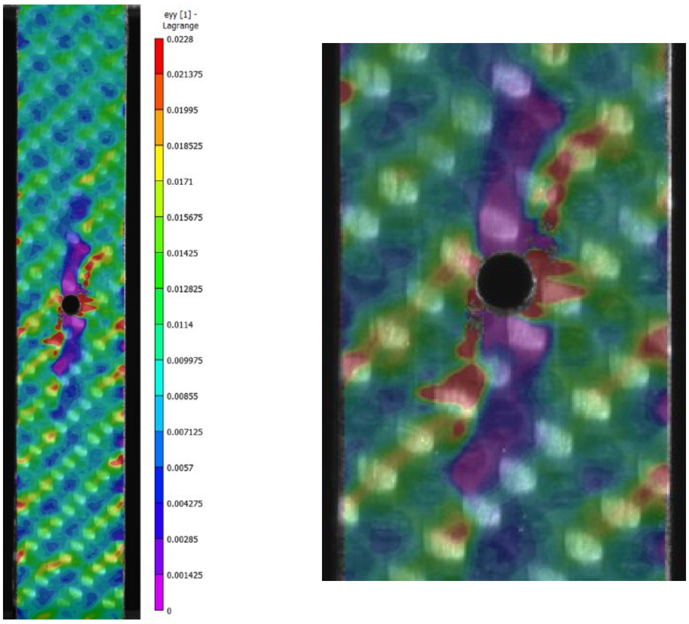

(a) (b)

Figure 1. Strain field in an open-hole woven composite specimen in uniaxial tensile test, obtained with Digital Image Correlation (DIC). (a) whole specimen, (b) detail of the notch area.

1.3 Statistical modeling of strength in composites

The Weibull distribution is the most widely used model to describe the strength of brittle materials. As touched on before, this strength theory assumes that the failure of brittle material is caused by statistically distributed flaws. In what is commonly known as the weakest-link principle, a component is as strong as its weakest element.

In its simplest, two-parameter form, the probability of failure F of a component after Weibull theory is expressed as:

$$F = 1 - exp\left[-\left(V\frac{\sigma}{\sigma_0}\right)^m\right], \tag{1}$$

where V is the volume of the component under uniform stress σ, σ_0 is its characteristic strength per unit volume of the material, and m is the shape parameter of the distribution (also known as Weibull modulus), associated with the variability of the material [42].

This statistical distribution has been applied with good results to model the strength of composite laminates [43,44]. It has been used as well to model the scaling of the strength of composite components observed in experiments [1,45]. The ultimate strength of individual carbon fibers has been observed to follow a Weibull distribution [46,47]. Statistical models for fiber bundles have been proposed to correlate the (microscale) strength of an individual fiber with (mesoscale) one of the fiber tows. For example, in [48] the unidirectional composite strength is described starting from the Weibull-distributed single fiber strength by a hierarchical bundle model.

The statistical method proposed in this work is developed from the one introduced in [49,50] to model the size effect in fatigue. This approach, which can be fruitfully adapted to describe at the mesoscale the problem in question, is based on the discretization of the part in sub-volumes which is operated by a finite element model. The weakest-link principle is then used to estimate the strength of the woven composite.

1.4 Overview of structure and modeling of woven textile composites

Textile composites are a subcategory of long-fiber-reinforced composites, in which the reinforcement is constituted by a large number of individual bundles of fibers (also known as tows) held together in a fabric by weaving or knitting. A fabric structure makes it possible to have fibers in multiple directions within a single ply. Among the most commonly encountered fabric weaves are plain weave, satin, and twill. In general, a more structured weave such as plain weave is more stable and symmetrical. A looser one such as satin is very drapeable, has lower crimping on the fibers, and is more porous for better impregnation. Twill, being between these two extremes, offers a good balance of properties [51].

Textile reinforcements are often chosen over unidirectional (UD) reinforcements due to their multiple advantages: they are cheaper to manufacture, more stable during processing, have superior drapeability, and better impact, fatigue, and corrosion resistance properties [52]. On the other hand, their complex structure, heterogeneous in fiber direction both in and out of the laminate plane, makes it more difficult to predict their behavior and model their mechanical response.

To address this, in the past decades there has been considerable effort to develop models that consider the structure of woven composites mesoscale level, at an ever-increasing level of detail. Among the earliest, the mosaic model, based on classical laminate theory by Chou and Ishikawa [53], which was further refined by several other studies [54–56]. While most works focused on plain weave fabric composites, there have been several on twill weave ones, both analytical [57] and numerical [58–61].

However, most of these models use a micro- or mesoscale-level approach as a stepping stone to obtain homogenized properties for the entire lamina, and the stress analysis is carried out at the macroscale. While woven composite plies can be successfully considered as a transversely isotropic material at the macroscopic scale, at a level close to that of their representative volume element (RVE), the effects of material heterogeneity could be non-negligible as they overlap with others, such as the already mentioned stress concentration from notches. The scale of notches at which this interaction takes place—a few millimeters—is exactly the one considered in most notched strength studies, since it is relevant to fastening applications. This interaction is evident in the experimental longitudinal strain field in the notched specimen in Figure 1. In Figure 2 the stress field in the same component has been obtained with a homogenized and a mesoscale orientation-aware model; both the distribution of the stresses in the ply and the maximum value (661 MPa versus 829 MPa) are vastly different.

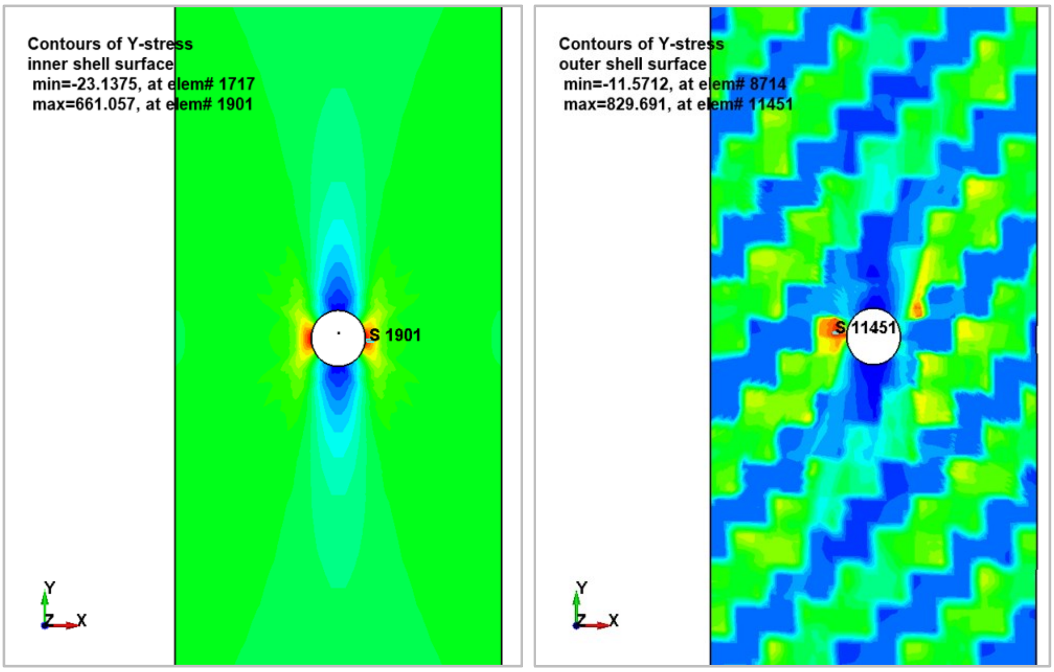

(a) (b)

Figure 2. FEM longitudinal stress field in an open-hole woven composite specimen in uniaxial tensile test, (a) with homogeneous material (b) with mesoscale-level oriented material.

Many modern 3D numerical models of fabrics are too complex to be applied to whole component analysis. This work used a new simplified mesoscale model to study open-hole tensile testing of composite coupons on a scale similar to that visible in Figure 2b.

1.5 Objectives of the thesis

The central objective of this work is to develop a statistical approach to describe the open-hole notch size effect on the ultimate tensile strength of woven composites. The methodology is applied specifically to a twill weave CFRP laminate material, with specimen width and width-to-diameter ratio selected as the scaling parameters.

Fundamental to the methodology is an innovative integrated experimental-numerical approach, that faithfully captures the full stress fields in the tested specimen. This enables the study of the hole size effect at the local level.

The proposed methodology involves the following steps:

1. Acquisition of experimental data through uniaxial tensile testing of open-hole specimens. Stereoscopic cameras and 3D DIC are used to record reliable full-field strain data.
2. Construction of a heterogeneous 2D shell finite element model, that contains mesoscale information on the local material orientation in the woven composite and is able to reproduce the strain and stress fields at the same level of detail. A semi-automated script, utilizing image processing and DIC position data, is used to map the material orientation of each individual specimen, subdividing it into the unidirectional tow material in the two orthogonal directions. The material properties for this model are determined through data-driven optimization rather than specialized testing. To this end, a FEMU method is developed, which minimizes the difference between the DIC-measured and FEM-calculated strain fields to calibrate mesoscale elastic properties.
3. Simulation of all the mechanical tests performed, using the mesoscale model calibrated with the DIC-FEMU process, to collect substantial full stress field data.
4. Development of a statistical model based on Weibull theory and the weakest link principle. Building on the newly obtained stress data, the model allows the study of size effect on the strength of the constituent tow material at the mesoscale level. Model parameters are determined via optimization, minimizing the error between empirical and model-calculated probabilities of failure.

The structure of the rest of this work follows the steps of the proposed methodology. Chapter 2 details the material selected, the manufacturing of the specimens, the mechanical tests performed, and DIC analysis. Chapter 3 describes the construction of the mesoscale FEM model, and the data-driven material parameters identification through the DIC-FEMU method. In Chapter 4 the results of the simulation of all tests using the optimized models are discussed, and they are used to reinterpret the size effect phenomenon at mesoscale. Chapter 5 details the development, tuning, and results of the statistical model of size effect on strength, which uses the stress field data obtained through the FEM models. Finally, Chapter 6 draws the conclusions of the study.

Chapter 2

Mechanical testing

This chapter details the mechanical testing campaign on the twill woven composite material. Testing was designed and carried out to provide the experimental data foundation for the following numerical and statistical study of the strength size effect in woven composites, as well as to provide experimental validation.

The chapter is organized as follows. In Section 2.1 the material and specimen design are described. The testing equipment and procedures, as well as the measurement systems and the DIC analysis, are discussed in Section 2.2. Finally, in Section 2.3 the results of the tests are presented.

2.1 Material and specimen characteristics

2.1.1 Test and specimen design

The test procedure and specimen designs were adapted from the open-hole tensile strength testing standard ASTM D5766M-11 "Standard Test Method for Open-Hole Tensile Strength of Polymer Matrix Composite Laminates" [62]. This method establishes a uniaxial tension test of a balanced and symmetric laminate specimen, with a centrally located hole. The testing procedure itself is largely derived from the ASTM Test Method D3039M-17 "Standard Test Method for Tensile Properties of Polymer Matrix Composite Materials" [63], widely used in the mechanical characterization of composite materials. The technical details of the test procedure used in this work are discussed in Section 2.2.

The specimens tested are rectangular coupons cut from a flat composite laminate and measuring 250 mm long (*l*) by 24 mm wide (*w*), with a hole in their center. A manufacturing drawing of a representative specimen is shown in Figure 3, with dimensions indicated by letters, which reference Table 1.

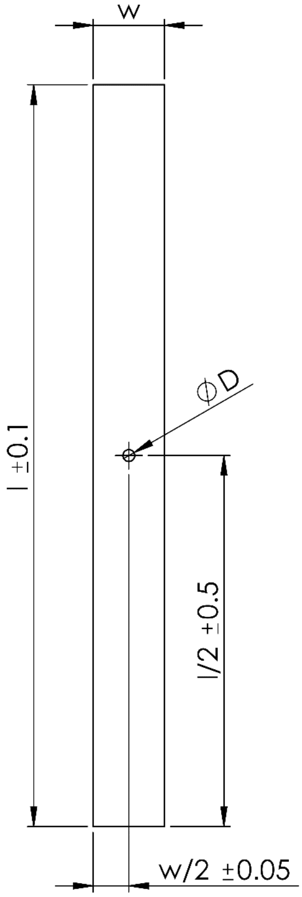

Figure 3—Drawing of a representative specimen. Refer to Table 1 for the numerical values of the dimensions for the various specimen types.

Table 1. Dimensions of all specimen types tested: length *l*, width *w*, hole diameter *D*, and width-to-diameter ratio.

Specimen	*l* [mm]	*w* [mm]	*D* [mm]	*w/D*
C20	250	24	Unnotched	—
C21	250	24	2 ±0.02	12
C22	250	24	4 ±0.04	6
C23	250	24	8 ±0.08	3
C31	250	36	3 ±0.03	12
C32	250	36	6 ±0.06	6
C33	250	36	12 ±0.12	3

Two different geometrical scaling factors were considered: width *w* and width-to-diameter ratio *w/D*. A total of six different notched specimen types were therefore tested. In addition, unnotched specimens in the narrower of the two widths were also manufactured and tested, to provide baseline results and for use in material characterization. Table 1 gives an overview of the nominal specimen dimensions and corresponding nomenclature. The values of the width-to-diameter ratio considered in this study span from three to twelve. The central value, $w/D = 6$, is the one suggested by ASTM D5766M. A factor of 2 was chosen to derive the other two ratios, so that hole size remains at a scale comparable to that of the fiber tows. At this scale there is the most interaction between material heterogeneity and notch, and the mesoscale analysis that will be undertaken is most significant.

Specimen nomenclature is codified as follows: the letter *C*, followed by a number indicating the width (*2* for 24 mm and *3* for 36 mm), and by a second number from 1 to 3 indicating increasing hole diameters (*1* for a *w/D* ratio of 12, *2* for a *w/D* of 6, and *3* for a *w/D* of 3). Each specimen is then individually numbered. For example, specimen *C23_1* is the first of the 24 mm wide specimens tested, with a hole diameter of 8 mm and a $w/D = 3$.

2.1.2 Material characteristics and manufacturing

The material system selected for this study is a carbon fiber-reinforced epoxy prepreg, supplied by Microtex Composites, and commercially known as *GG630 T125 12K 37%*. This composite material is quite versatile and has diverse applications, including the automotive, sports equipment, nautical, and civil engineering fields. Although a prepreg was used in the production of the specimens, the base fabric is also suited to numerous other production processes such as hand lay-up, vacuum infusion, and RTM.

More in detail, the GG630 T125 12K reinforcement is a carbon fiber fabric, woven in a 2 × 2 twill pattern and with an area density of 630 g/m^2. Both warp and weft consist of 12K-filament bundles of carbon fibers, resulting in a balanced fabric. The matrix is a thermosetting epoxy resin, commercially known as E3-150N.

A laminate with [0/90/0] stacking sequence was manufactured by hand layup on a flat metal mold and autoclave curing, following the curing cycle shown in Figure 4. The resulting composite plate is shown in Figure 5a. The average cured thickness for the laminate measured 2 mm.

The specimens were cut from the composite plate using a Kent KMV 11 EL CNC vertical milling machine. While the specimens were still joined to the plate, circular holes with the specified diameters were machined into them, using drill bits. A CNC machine was preferred to other machining methods, such as waterjet cutting, for its ability to provide precise location tolerances of the hole within the specimen. The composite plate during the milling process is shown in Figure 5b.

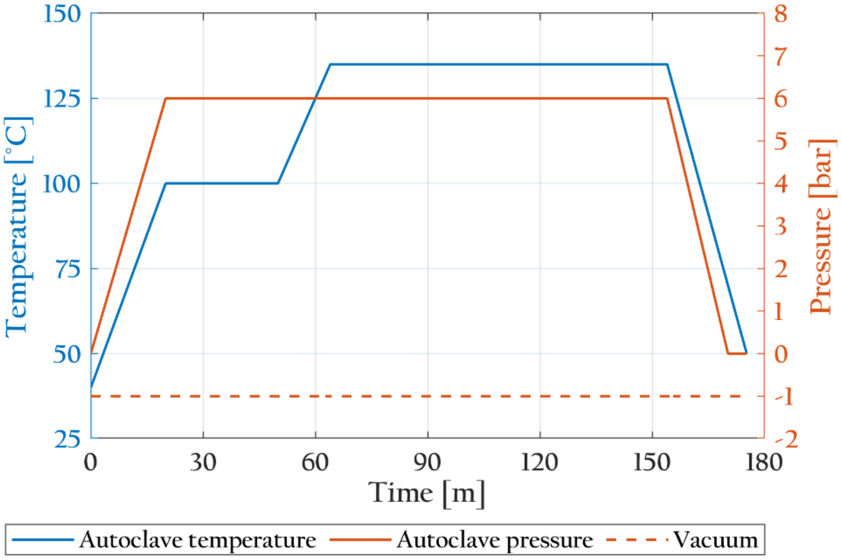

Figure 4. The autoclave curing cycle used in the production of the specimens.

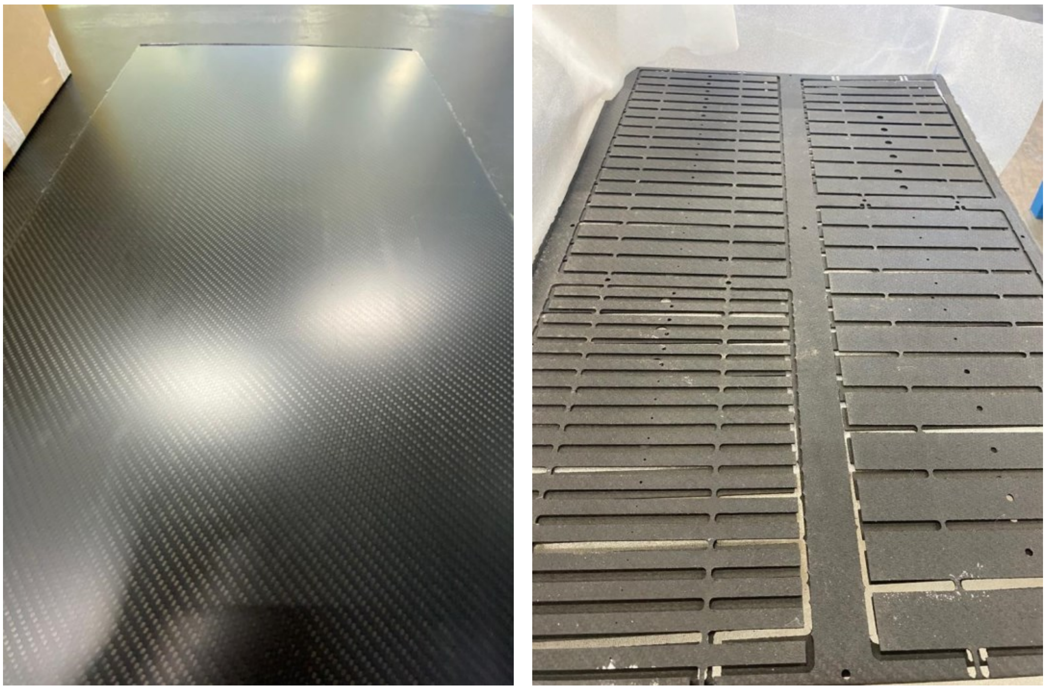
(a)
(b)

Figure 5. Manufacturing of the specimens: (a) the composite plate during quality control, (b) the same plate during the milling operations.

2.2 Tensile testing

2.2.1 Equipment and setup

Uniaxial tensile tests on the specimens were carried out on an Instron 8001 hydraulic universal testing machine in the laboratory of the Department of Mechanical and Aerospace Engineering of Politecnico di Torino. This machine is equipped with hydraulic grips with serrated faces.

Figure 6. The testing setup.

During the tests, the following measurements were recorded:

- Load, using the testing machine's ±100 kN Instron load cell.
- Crosshead displacement, using the testing machine's onboard transducer.
- Position, displacements, and strains on the whole specimen surface, using Digital Image Correlation.

A stereo camera system was employed to image the entirety of the specimen throughout all tests. The system was based on two Basler Ace acA4096-30um cameras, each equipped with a 1-inch Sony IMX267LLR 8.9 MP monochromatic CMOS sensor. A lens selector software tool, MachVis, was used to identify the best lens combination for the application. Specifically, this was a Rodenstock Rodagon 80 mm *f*/4 C-mount lens paired with a 48 mm long extension tube and a manual focusing ring. The acquisition system was completed by a Hedler DX15 daylight flood light with a 150 W HMI gas discharge lamp, necessary for uniform illumination of the specimen. Figure 9a shows a specimen in the test fixture as imaged by the principal of the two cameras, and Figure 6 an overview of the testing setup.

A schematic of the acquisition and test control system is visible in Figure 7, and its functioning will be described in the following. At the center, a data acquisition unit (DAQ) links together the testing machine side of the system with the DIC imaging system. Each side uses a workstation for control by the operator and data storage. The software Vic-Snap 9 by Correlated Solutions was used on the DIC workstation for camera control and data acquisition. The DAQ unit, based on the programming received from the DIC workstation, triggers at an operator-selected frequency the two stereo system cameras through an I/O connection to take pictures. At the same time, it acquires the load cell and crosshead displacement signals from the testing machine, through analog inputs, and outputs it to the acquisition workstation. The images acquired by the cameras are transmitted to the acquisition workstation directly through USB 3.0 cables. This allows recording load and displacement data perfectly synchronized with each captured frame and, after DIC post-processing, with full-field specimen strain information

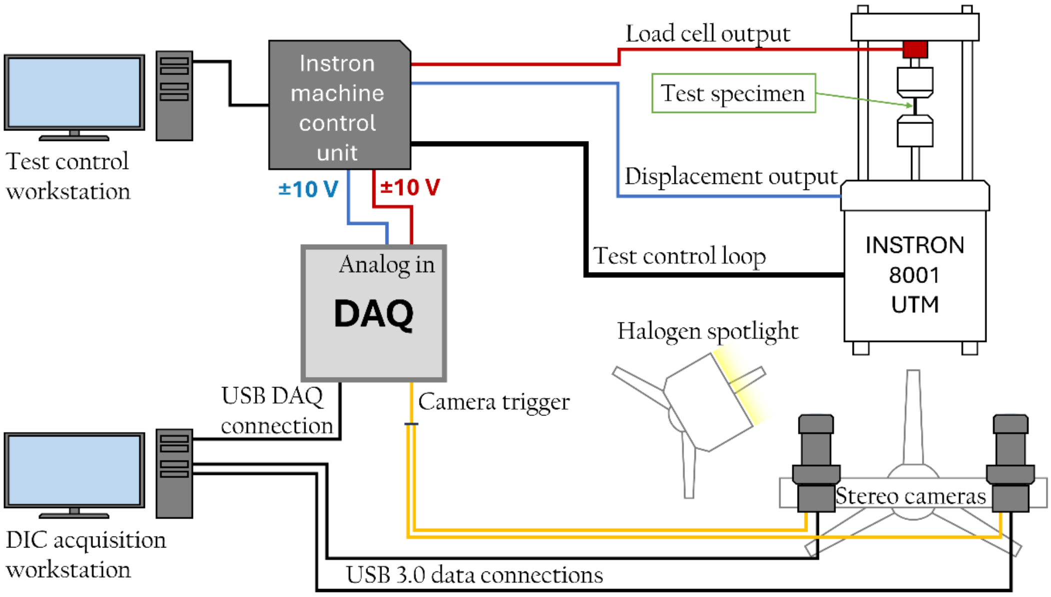

Figure 7. Diagram of the acquisition system.

DIC analysis requires the specimen surface to be covered in a high-contrast random pattern. The specimens were therefore airbrushed with a black speckle pattern on a white base (Figure 9b). Using a professional airbrush ensures reproducible speckling results, as this tool can be consistently set up for every test with the same air pressure, nozzle diameter, air, and paint flow. This provides both the ability to achieve a desired speckle fineness and to apply it consistently to different specimens, even if not tested at the same time. Proper technique for speckle application involves maintaining a constant distance from the specimen and constant overlap in the spraying passes. If such care is taken, the resulting speckle is very uniform. For this work, the speckle pattern was applied using an airbrush with a nozzle diameter of 0.2 mm. The resulting pattern has a mean speckle diameter of 0.25 mm.

No tabs were bonded to the specimens, since the open-hole stress concentration was sufficient to induce failure on the midpoint of the free span. However, excessive grip pressure can still cause a significant multiaxial stress state in the specimen in the vicinity of the fixture, and invalidate the uniaxial tension hypothesis as well as alter the strain field recorded by DIC. To avoid this, through set-up testing of sacrificial specimens, the grip closing pressure was set to the lowest value which guaranteed no specimen slippage during the whole test.

2.2.2 Procedure

Several operations needed to be conducted in advance of the tensile test proper:

- Width and thickness of all specimens were measured, in three different locations along the free span as instructed by ASTM D3039M. The average of these three measurements was considered for the calculation of mechanical properties. The length of the free span of the specimen was defined by the distance between the test machine grips, which was set at 145 mm when crosshead displacement was zeroed at the start of the testing.
- For stereo system calibration, a calibration target with 7 mm grid spacing was imaged in various positions and angles inside the field of view of the cameras. Example calibration images as captured by the two cameras are visible in Figure 8.

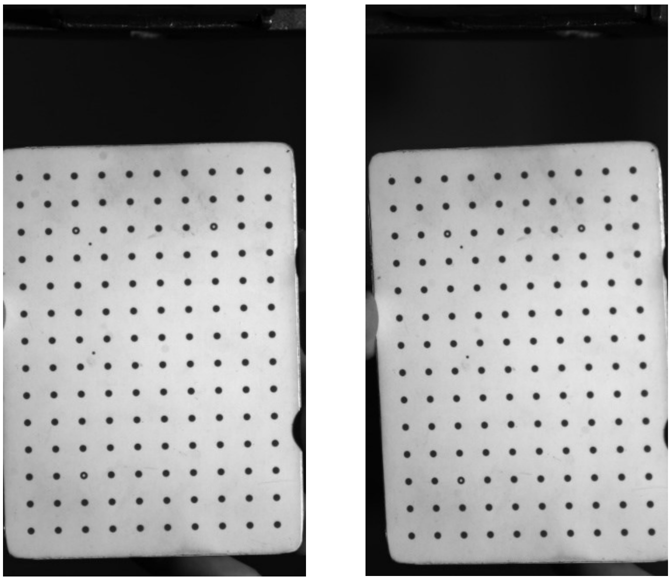

Figure 8. Stereo camera system calibration images.

- Pictures of each bare specimen on the test fixture were taken with the DIC cameras before applying the base paint and speckle pattern (Figure 9), in the same position where it would be placed during testing. These pictures were later used to build the FEM model, as will be described in Chapter 3.

The tensile tests were conducted in displacement control, at a constant, quasi-static displacement rate of 2 mm/min. The camera recording frame rate— and therefore also load and displacement recording rate—was set to 4 fps. The test was ended by the failure of the specimen. At least three specimens were tested for each specimen type.

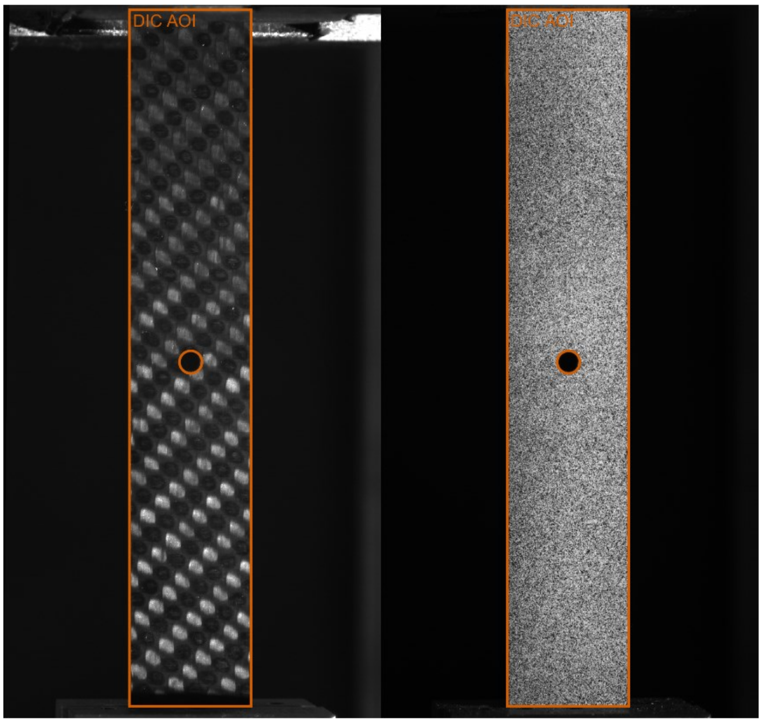

Figure 9. The same specimen in the test fixture, without and with speckle pattern.

2.2.3 DIC post-processing

After having been recorded, the speckle images of the tested specimens were processed using Correlated Solution's VIC 3D 9 commercial digital image correlation software.

The post-processing procedure used and the parameters selected will be briefly described here. The first step in the processing was the calibration of the stereo camera system, performed via a utility of the software (Figure 10). The dots on the target grid are matched on each pair of camera images, and calibration parameters are calculated from all images and averaged. A score is calculated for each pair, representing the difference in pixels from the calibrated model-calculated position of the dots and the actual registered one. In this case, the pairs of images with the highest scores were manually removed from the sequence, until reaching a satisfactory calibration score under 0.04.

The same calibration data could be saved and used for all specimens tested. Care had to be taken to use the autocorrect calibration function before processing each test, to account for slight variations between the tests due to minor shifts in the relative position of the cameras and specimen. The area-of-interest (AOI) where image correlation was performed was the whole visible speckled camera-facing surface of the specimen, defined in the software as a rectangle from which a circle (the notch) is subtracted.

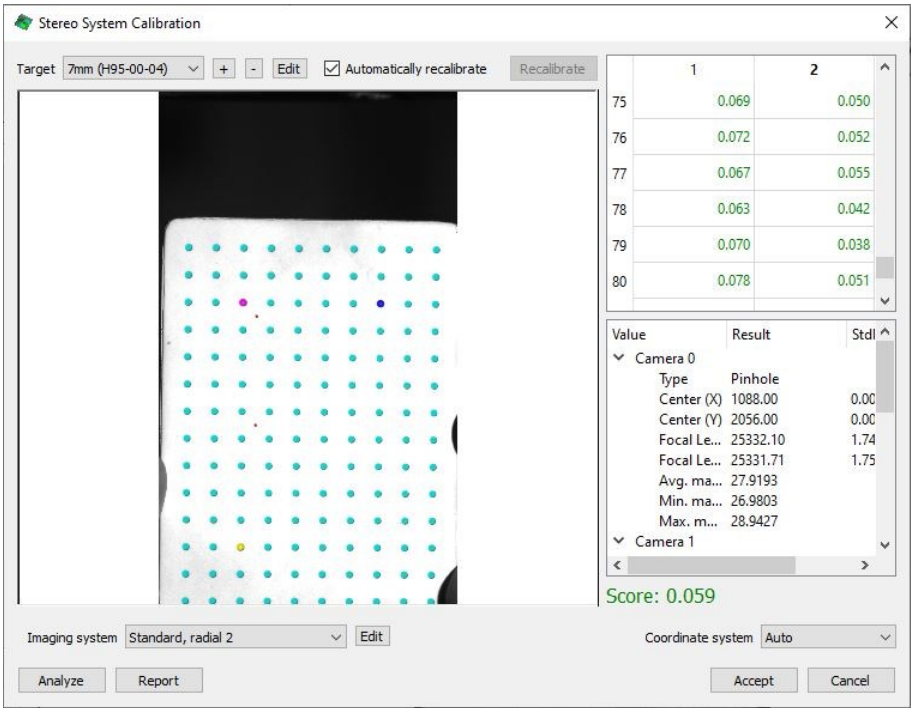

Target 7mm (H95-00-04)

☑ Automatically recalibrate

	1	2
75	0.069	0.050
76	0.072	0.052
77	0.067	0.055
78	0.063	0.042
79	0.070	0.038
80	0.078	0.051

Value	Result	Stdl
Camera 0		
Type	Pinhole	
Center (X)	1088.00	0.00
Center (Y)	2056.00	0.00
Focal Le...	25332.10	1.74
Focal Le...	25331.71	1.75
Avg. ma...	27.9193	
Min. ma...	26.9803	
Max. m...	28.9427	
Camera 1		

Score: 0.059

Imaging system Standard, radial 2

Coordinate system Auto

Figure 10. Stereo DIC calibration utility.

The definition of the AOI does not require precision, as the correlation of subsets where no speckle is present is lost when processing the first frame captured, and does not affect the rest of the analysis.

A built-in VIC 3D tool was used to select subset size (Figure 11). The tool helps identify the minimum size of subset which guarantees a distinctive enough pattern to match in each frame, for an assumed level of noise from the camera. An optimal value of subset size of 31 pixels was used for all specimens, attesting to the consistency of the speckling procedure used. The step between the subsets was set at 6 px, which is less than 1/3 of the subset size following recommendations by Schreier *et al.* [34].

After the selection of the AOI and of the subset parameters, the correlation analysis was run. No initial guess was required since the specimen geometry does not feature surface curvature. The main correlation options used in the analysis are visible in a screen capture of the selection window in Figure 12a.

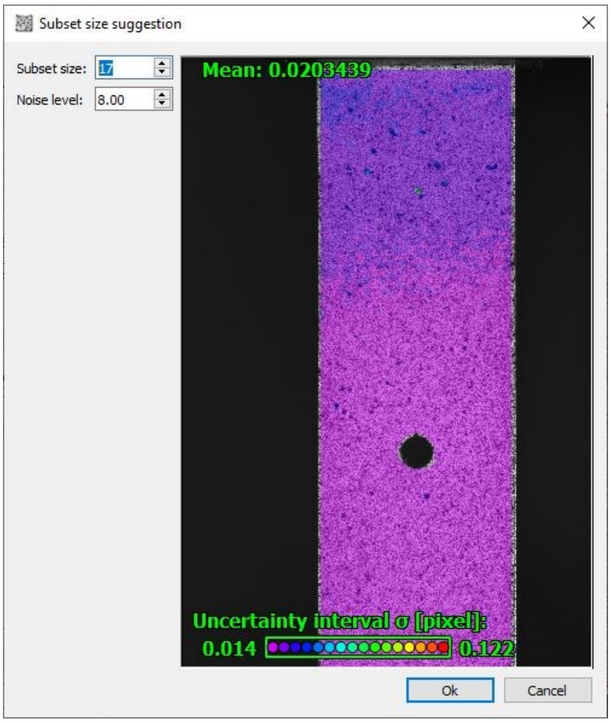

Subset size: 17
Noise level: 8.00
Mean: 0.0203439
Uncertainty interval σ [pixel]:
0.014 0.122

Figure 11. Subset size selection.

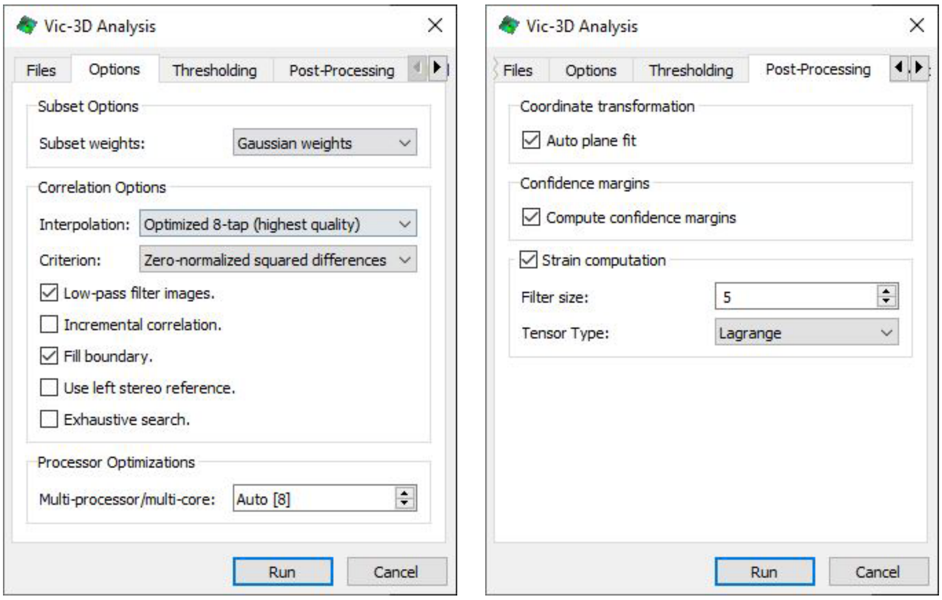

Subset Options
Subset weights: Gaussian weights
Correlation Options
Interpolation: Optimized 8-tap (highest quality)
Criterion: Zero-normalized squared differences
☑ Low-pass filter images.
☐ Incremental correlation.
☑ Fill boundary.
☐ Use left stereo reference.
☐ Exhaustive search.
Processor Optimizations
Multi-processor/multi-core: Auto [8]

Coordinate transformation
☑ Auto plane fit
Confidence margins
☑ Compute confidence margins
☑ Strain computation
Filter size: 5
Tensor Type: Lagrange

(a) (b)

Figure 12. Digital image correlation analysis parameters in VIC 3D: (a) correlation options and (b) post-processing options.

The following options were selected:

- The Gaussian weights option applies center weighting to the subset pixels, and improves the balance of spatial and displacement resolution.
- 8-tap sub-pixel spline interpolation gives better displacement results at the cost of extra computational time.

- The zero-normalized correlation criterion has the advantage of being unaffected by any lighting changes during the test.
- Low-pass filtering removes high-frequency noise from the image that would produce aliasing in smaller speckles.
- Lastly, the fill boundary option was very important in this application of DIC. When this box is checked, VIC 3D attempts to fill the area between the last full-sized subset and the edge of the AOI, where no information is available, by using smaller subsets. This recaptures very meaningful information, since strain concentration is maximum on the edge of the notch.

Thresholding parameters, used to remove suboptimal data, are not reported here as test conditions were ideal and no changes in the default values were necessary.

For post-processing, calculation of the Lagrange strain tensor was selected, with a filter size of 5. This is a decay filter that smooths the calculated strains over the selected number of data points equal to filter size, thereby reducing noise.

The relevant variables output by VIC 3D for each data point in each frame were:

- x and y [pixel], position in the raw image.
- X, Y, and Z [mm], position in the calibrated frame of reference. The X-axis is the horizontal axis, Y the vertical axis along which tensile load is applied, and Z the out-of-plane axis.
- Sigma [pixel], the standard deviation of confidence in the correlation. It is 0 if correlation is perfect, and takes higher values if either noise or decorrelation occur.
- u and v [pixel], the x- and y-axis displacement from the reference image.
- U, V, and W [mm], the X-, Y-, and Z-axis displacements from the reference image in the calibrated frame of reference.
- e_{xx}, e_{yy}, and e_{xy}, strains in the X-direction, Y-direction and in shear.

No further post-processing was carried out in VIC 3D. All data was exported in MATLAB format for analysis.

2.3 Testing results

2.3.1 Characterization of the homogeneous material

A material characterization of the whole laminate was conducted as an initial step using the unnotched specimens, to get baseline mechanical properties of the homogenized composite material. The ASTM D3039M-17 test standard was followed to obtain tensile properties, and the test procedure was similar to that used for the open-hole testing. ±45 angle-ply specimens were also tested with a similar procedure, to obtain shear modulus according to test standard D3518M-18 “Standard Test Method for in-Plane Shear Response of Polymer Matrix Composite Materials by Tensile Test of a ±45° Laminate” [64]. Four repeats of the tensile and shear test were carried out, on unnotched, 24 mm wide specimens named respectively from *C20_1* to *C20_4* and from *A20_1* to *A20_4*.

The load-displacement and engineering stress-strain curves for the unnotched tensile specimens are plotted in Figure 13. Engineering stress was calculated by dividing the recorded load by the measured cross-section of the specimen, while the strain is the average of recorded DIC longitudinal ε_{yy} strain over the entire area-of-interest on the surface of the specimen.

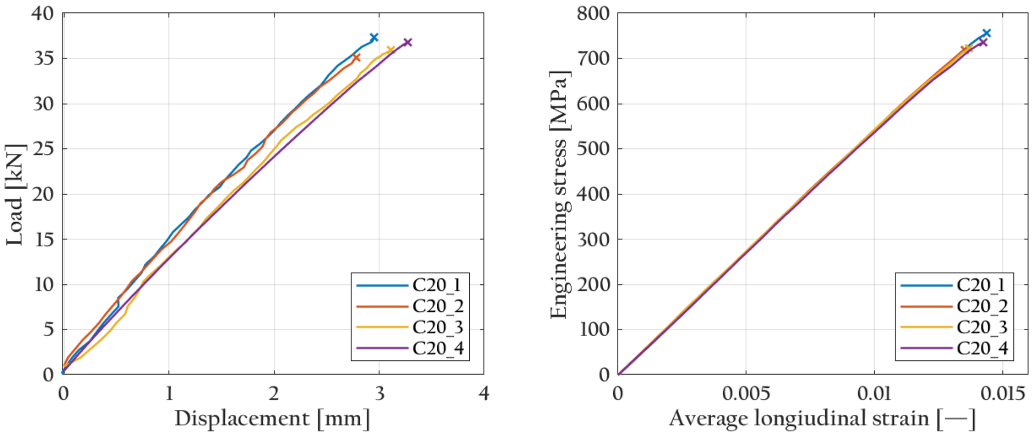

(a) (b)

Figure 13. Load-displacement curves (a) and stress-strain curves (b) for the unnotched specimens, tested per ASTM D3039M-17.

The experimental curves are linear, with limited non-linearity immediately before failure, and repeatability of the results is good. The average tensile mechanical properties of the laminate are collected in Table 2, together with their standard deviation and coefficient of variance. At the macroscale the material is orthotropic, and therefore the properties are identical in the two fiber directions (0° and 90°).

Table 2. Tensile properties of the laminate, determined per ASTM D3039M-17.

Property	Mean value	Standard deviation	COV %
E	54.34 GPa	0.52 GPa	1.0
UTS	732.80 MPa	0.02 MPa	2.3
$\boldsymbol{\upsilon}$	0.078	0.016	20.1
G	3.32 GPa	0.10 GPa	3.1

2.3.2 Experimental open-hole testing curves

All tested specimens experienced brittle failure mode along a line passing through the hole. Some examples of failed specimens are shown in Figure 14. Load-displacement curves recorded for the notched specimens are plotted in Figure 15. For ease of interpretation, an image of the corresponding type of specimen is shown next to each cluster of failure points. This plot uses data from the test machine's load cell and displacement transducer. Here, the different specimen types display different stiffnesses and maximum loads. Both properties decrease following hole size, as expected. Stress-strain curves for the notched specimens tested are reported in Figure 16. The longitudinal engineering stress used in this plot is calculated per ASTM D5766M-11, by dividing the recorded load by the gross (unnotched) cross-section of the specimen. The longitudinal strain is calculated by averaging the DIC ε_{yy} strain over the entire area-of-interest.

Regardless of hole diameter, all specimens of the same width show a similar tensile modulus. On the other hand, the nominal ultimate tensile strength of the specimens is affected by hole size. Repeatability is good, with specimens showing consistent stiffness and relatively low dispersion in the failure stress. All specimens showed mostly linear behavior throughout the test. The brittleness of this material is apparent from the stress-strain curves, which are linear until sudden failure, a typical behavior from a high-modulus fiber composite.

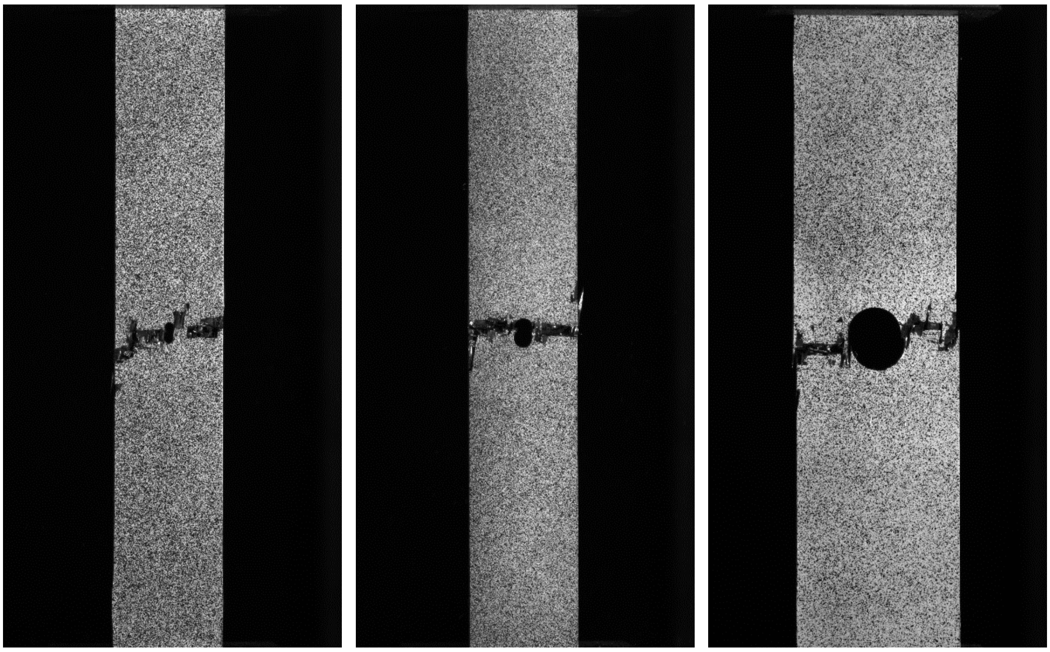

(a) (b) (c)

Figure 14. Specimens after failure. (a), *C21_2*; (b) *C22_1*; (c) *C33_2*.

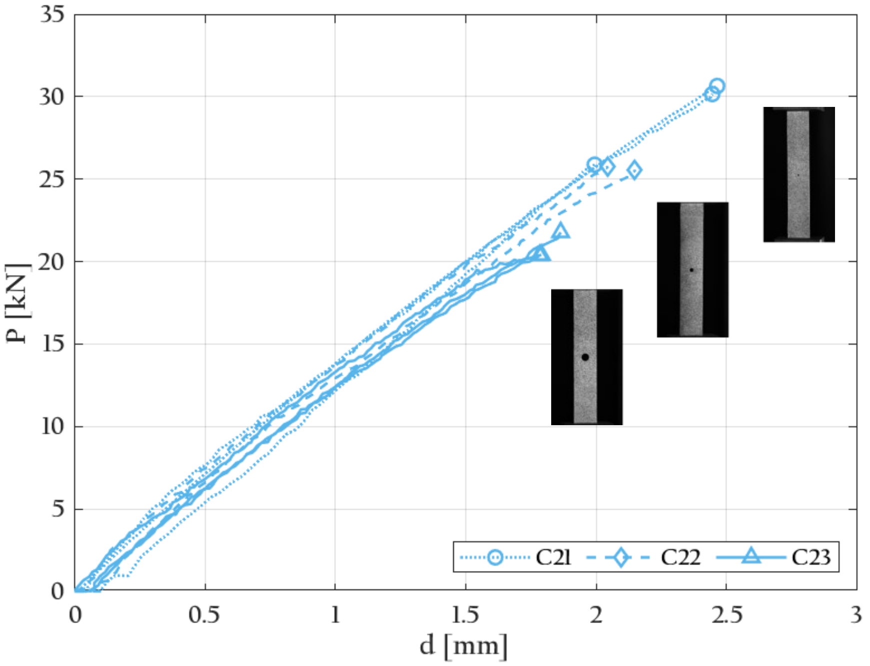

(a)

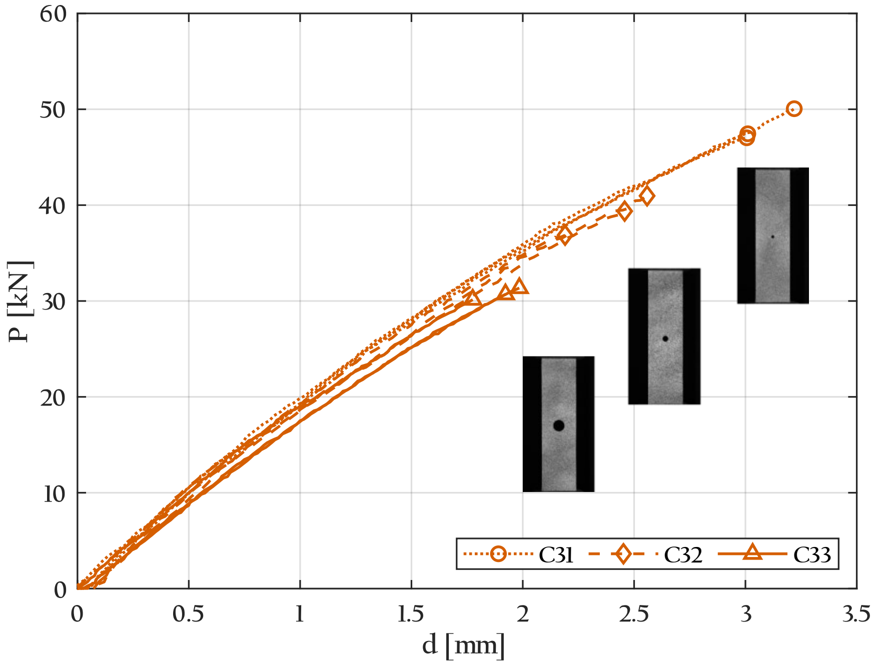

(b)

Figure 15. Load-displacement curves for the notched specimens, (a) 24 mm wide, (b) 36 mm wide.

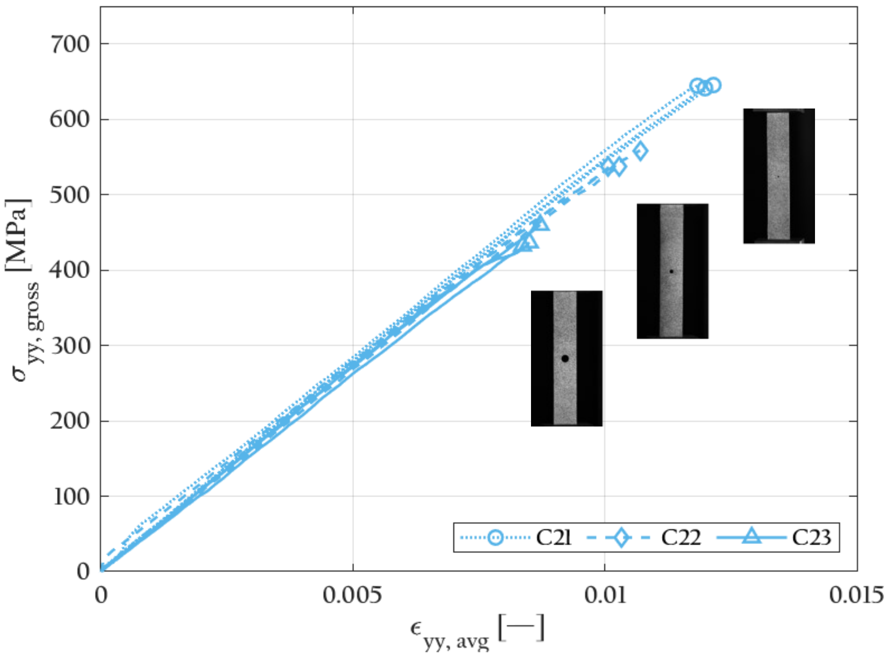

(a)

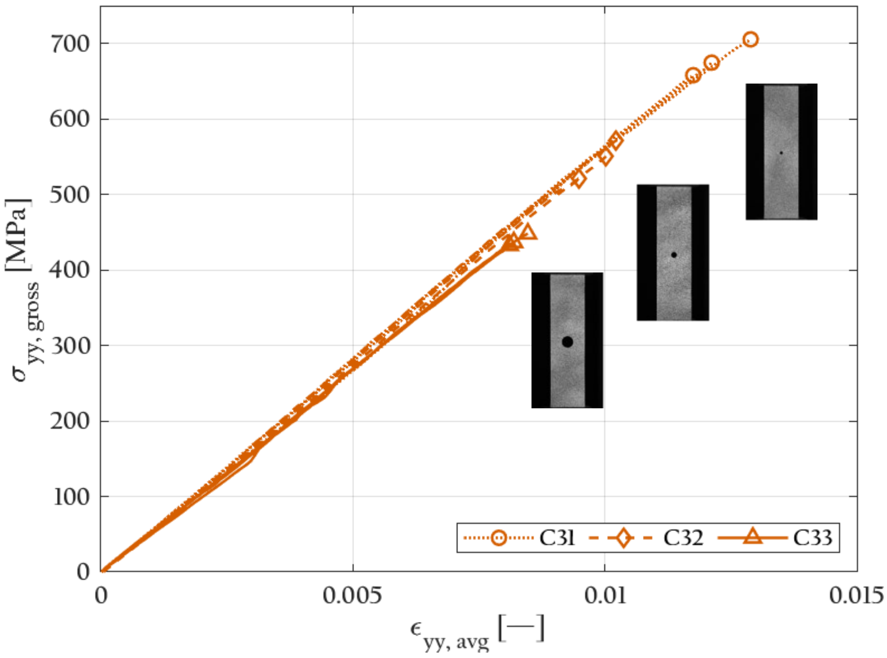

(b)

Figure 16. Stress-strain curves for the notched specimens, (a) 24 mm wide, (b) 36 mm wide.

2.3.3 Analysis of the DIC-determined strain field

An example of DIC-determined strain fields for a notched specimen is shown in Figure 17. Longitudinal strain is the highest in entity overall. In this strain direction, the characteristic structure of 2 × 2 twill fabric, with diagonal bands of vertical tows alternating with horizontal tows, is translated into clearly visible high-strain diagonal bands, corresponding to the longitudinal tows. Less intense high-strain bands along the opposite diagonal direction are due to the intermediate 90° angle ply. Examining the area around the round notch, it can be observed how this diagonal material distribution and the open-hole interact. The high strain caused by the notch extends into the longitudinally oriented material. The strain concentration is notably not symmetrical with respect to the hole. Such a strain distribution cannot be adequately described using a homogeneous material model.

Moving on to the transverse strain (Figure 17b), its values are the lowest and show little banding and concentration effects. Finally, the shear strains (Figure 17c) are mostly generated in 45° directions around the hole and fall close to zero moving away from it. The shear strain field again appears to be less affected by the material distribution than the longitudinal one.

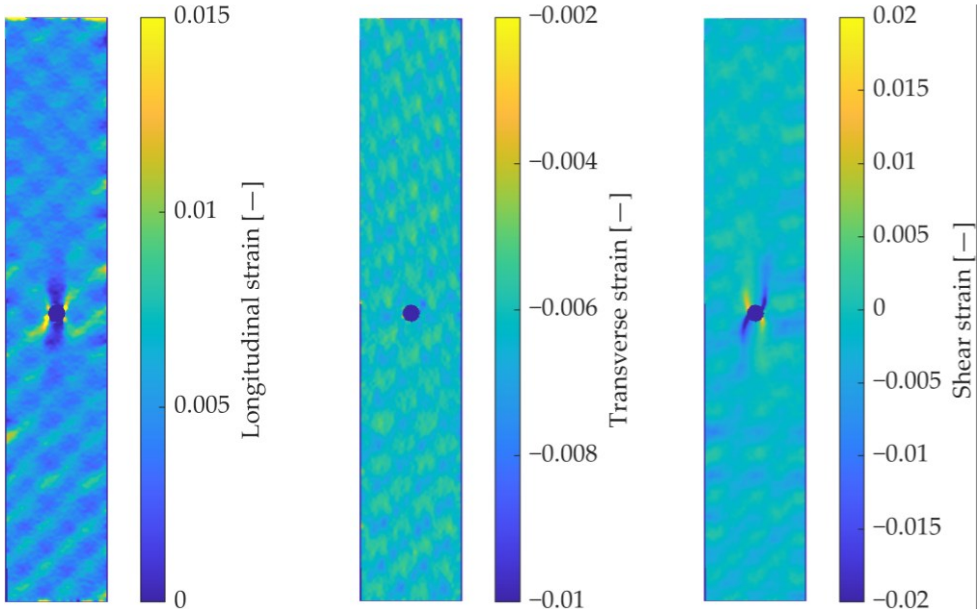

(a) (b) (c)

Figure 17. DIC-determined strain fields: (a) longitudinal strain, (b) transverse strain, (c) shear strain.

In the following chapter, these strain maps will be used to determine the tow-level elastic parameters of the material.

Chapter 3

Data-driven calibration of the mechanical properties

In this chapter, the mesoscale modeling of the woven composite and relative methodology for identification of the material properties via a FEMU method will be detailed. This data-driven identification process exploits DIC strain data from tensile testing of a plain, unnotched C20-type specimen. Essential to the process is a FE model able to reproduce the strain field with a resolution on par with that of DIC, which in turn requires knowledge (a "mapping") of the local material orientation in the composite.

Section 2.13.1 illustrates the strategy adopted to model the woven composite. The mapping of the material orientation necessary for this model is described in Section 3.2. The implementation of the finite element model is described in Section 3.3. Lastly, Section 3.4 presents the FEMU method for the identification of the material properties and its results.

3.1 Modeling of the woven composite

In woven composites a complex strain distribution can be observed with full-field measurement methods, which originates from the interlocking structure of orthotropic bundles of fiber (known as tows) in vertical (warp) and horizontal (weft) directions. This structure is visible as it appears on the surface of the specimen in Figure 18a, and schematically in Figure 18b.

For a model to correctly predict the strain and stress localization, this distribution must be adequately described. A common way to model composite laminates in a simplified form is using 2D shell elements. In such a model, the mesoscale-level heterogeneity can be described by locally changing material directions—or, in other words, dividing the component into two orthotropic materials with identical properties and orthogonal orientations.

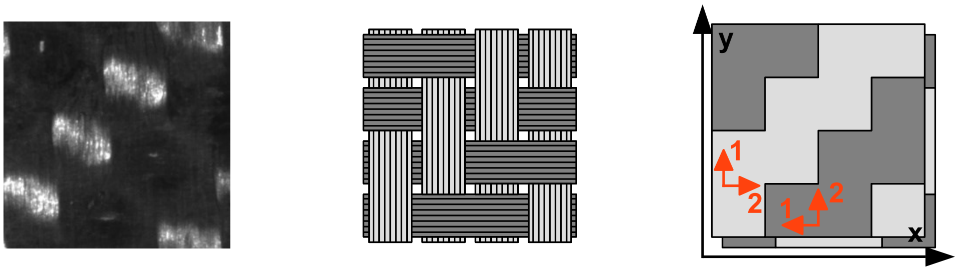

(a) (b) (c)

Figure 18. A 2 × 2 twill weave unit cell. (a) DIC camera imaging of the specimen; (b) idealized representation; (c) 2D model, with oriented material and two layers to represent the fabric structure. Global and local material directions are shown in black and orange respectively.

Furthermore, in the most simplified representation, the cross-section in any point of a twill fabric is constituted by a warp and a weft tow overlapping with perpendicular fiber directions, as visible from the micrograph in Figure 19. This can be recaptured in the model by juxtaposing two layers with opposite material distributions (Figure 18c), constructing the most simplified 2D model of the three-dimensional woven structure. In this work, this was implemented as two layers of integration points in a single shell. This approach allows a sizeable reduction in computational effort when compared to more standard multiscale models. Properties of the constituent material, while not identifiable through classic mechanical testing, have been obtained by minimizing the difference between the experimental and numerical full-field strains.

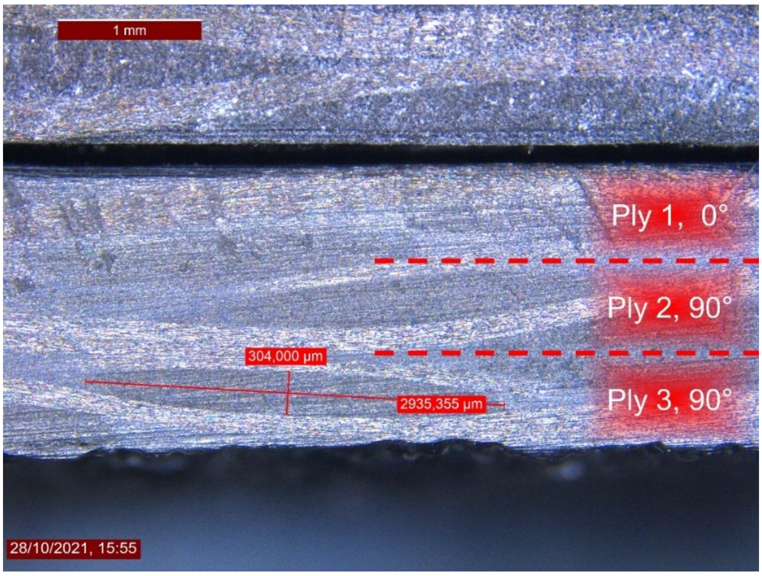

Figure 19. Micrograph of the cross-section of the tested laminate

The reference systems used in the following are two. With reference to Figure 18c, $x - y$ is the global system, consistent with the definition used discussing DIC processing in Chapter 3, where y is the tensile loading direction; while $1 - 2$ is the local material orientation, where 1 is the "fiber direction" and 2 the "matrix direction". For example, the longitudinal stress in the loading direction σ_{yy} is, depending on material orientation, a fiber direction stress σ_1 in vertical tows or a matrix direction stress σ_2 in horizontal tows.

3.2 Construction of the material map

The stereoscopic 3D DIC data obtained as described in Section 2.2.3 comprises position, displacement, and strain. This section describes how local material orientation (a "material orientation map") is added to this collection of information. The semi-automated image processing-based procedure, summarized in Figure 20, is the subject of this section.

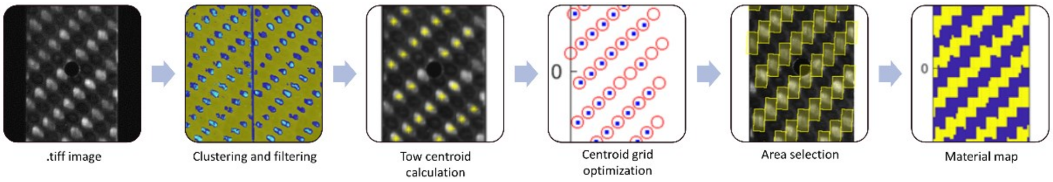

Figure 20. Construction of the material map.

3.2.1 Principle of operation

The reflectivity of carbon fibers is directional and depends on the angle of incidence of light. With reference to the bidirectional reflectivity diagram in Figure 21, it is maximum when the beam is parallel to the fiber direction, and the angle θ_i is null [65]. It is maximum as well as when the light source is perpendicular to the source, and the incidence angle φ_i is null.

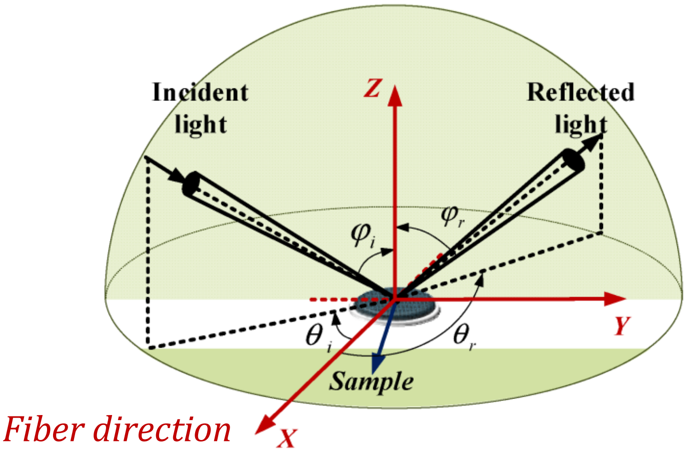

Figure 21. Bidirectional reflectivity [66].

It is therefore possible, by appropriately placing a light source and camera, to make the tows of fibers emerging to the surface of the woven composite specimen appear brighter when oriented along the vertical direction than in the horizontal one. This may be appreciated in the specimen pictured in Figure 22.

This difference in brightness can be exploited to identify the orientation of carbon fiber tows in an image of the specimen captured with the camera system described in Section 2.2.1. Each image recorded during the test is a 4112 × 2178 array of integers, codifying the grey level with values between 0 (white) and 255 (black). Using a clustering algorithm operating on the grey level, the tows of fibers oriented in the vertical direction can be isolated in the image. For each separate cluster, the position of its centroid within the array, i.e. its position within the image, can be computed. The centroids of the clusters thus isolated are assumed to be the centers of the fiber tows. The remaining information needed to build a material orientation map is the position of every tow centroid within the specimen, which is provided by 3D DIC data.

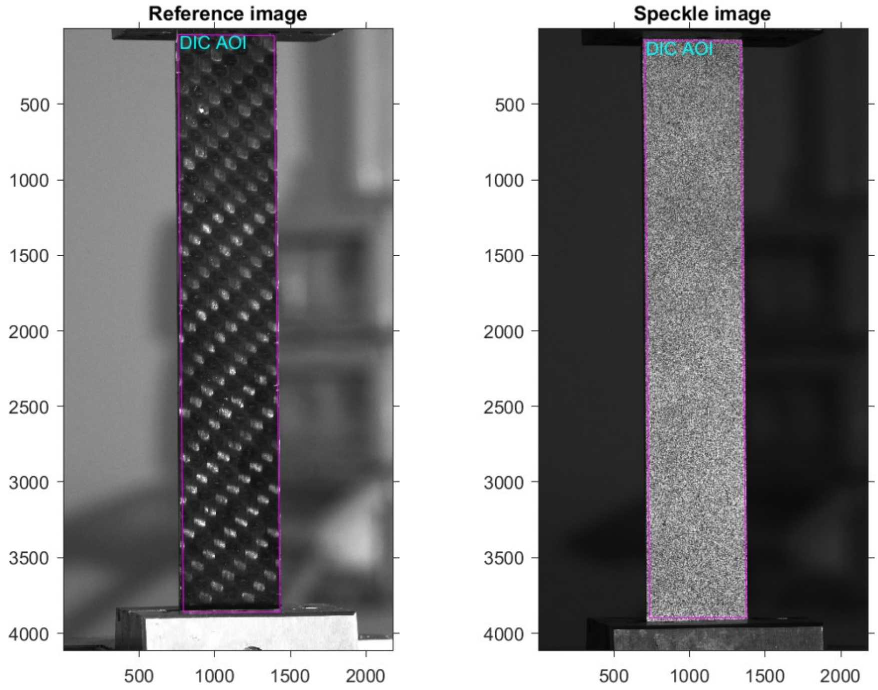

Figure 22. Reference specimen image and speckle image, with aligned reference systems.

The position in both pixels (arrays x and y) and in millimeters (arrays X and Y) within the image are known for every subset for which image correlation has been run. These may be interpolated and processed so that the position within the specimen is known for every pixel in the image, as visible in Figure 22, where the DIC area-of-interest is overlayed on both the speckled and non-speckled specimen.

3.2.2 The material mapping algorithm

This section describes in detail the algorithm for the construction of the material map, which was implemented in MATLAB R2021b.

The procedure starts by importing the image of the specimen and the DIC position data, which are then centered in the midpoint of the specimen. Next, the *kmeans* function, native to MATLAB, is used to perform a k-means clustering of the specimen image. The k-means clustering algorithm, also known as Lloyd's algorithm [67], iteratively partitions a number of data points in exactly k clusters. In this case, the data points are the pixels of the grayscale image, which are divided into $k = 3$ clusters. These roughly correspond to the vertically oriented fiber tows, horizontally oriented tows, and surrounding matrix. Of the three clusters, the one containing the lowest amount of data points corresponds to bright areas in the image, i.e. the vertical tows. By merging the two other clusters, good tow identification is achieved. The clustered image is shown in false colors in Figure 23a, with blue corresponding to the vertical tows. A Gaussian filter is then applied to reduce noise (Figure 23b).

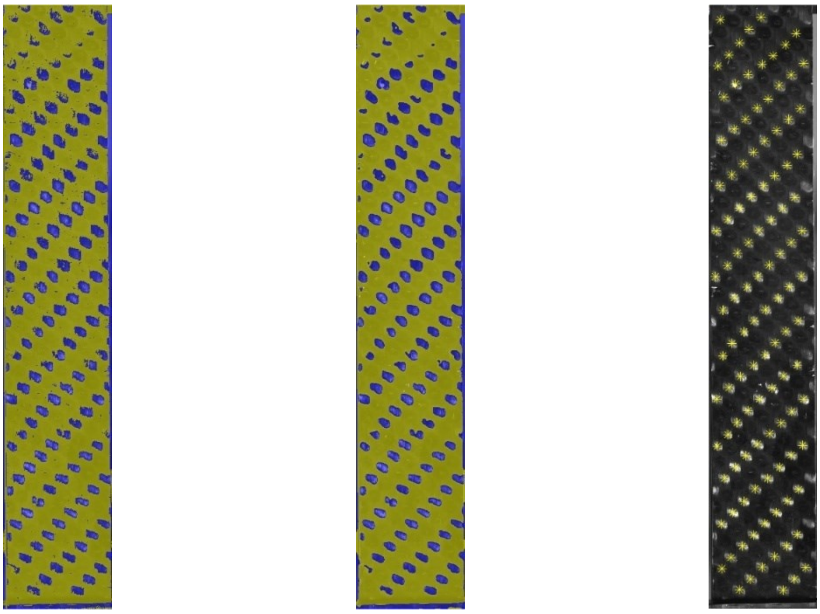
(a) (b) (c)

Figure 23. Tow identification process on the grayscale specimen image. (a), after k-means clustering; (b) after filtering; (c) overlaying in yellow of the cluster centroids on the original image.

The clustered image is then binarized and, using the MATLAB function *regionprops*, the "tow" cluster is partitioned into individual blue regions in Figure 23b, each corresponding to a vertical tow. This function also calculates the position of the centroid of each region. The centroids are visible in Figure 23c, overlayed over the original grayscale image. A manual step is subsequently needed, to remove false positives around the edges of the specimen, and centroids corresponding to incomplete tows on the edges of the specimen. Finally, tow centroid positions are converted from pixel coordinates to in-specimen metric calibrated $X - Y$ coordinates.

The map of tow centroids thus obtained is, however, not exact. There are variations in the position of each, due to their imperfect shape, minor variations in weave geometry during the production process, and measurement errors. However, an exact grid is preferable for two main reasons. First, regardless of shape, all fiber tows contain the same number of fibers, and are therefore best represented by the same amount of material. Second, the purpose of this map is not to analyze the quality of the fabric weave, but to provide material information to a FEM model, which is geometrically exact.

A uniformly spaced grid of calculated tow centroids is therefore constructed and fitted to the experimentally individuated centroids with an optimization algorithm. An example of this is visible in Figure 24a, with the identified tows plotted as blue dots and the grid in red circles. The spacing parameters, i.e. the distance between two adjacent centroids, are first estimated from of three diagonal rows of centroids. The selection of these three rows is a second operation requiring human intervention. An optimization process is then used to determine the correct spacing parameters of the grid, as well as an in-plane rotation angle. This optimization algorithm works by minimizing the sum of the distances between each experimentally individuated identified centroid and the closest centroid in the exact grid.

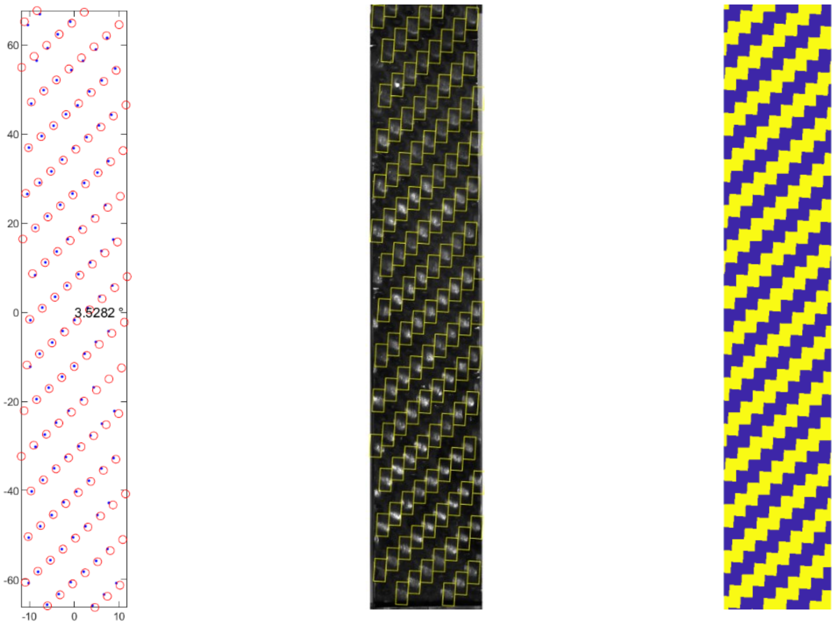

(a)

(b)

(c)

Figure 24—Construction of the material map: (a), best fit of a uniformly spaced grid to the experimentally identified centroids; (b) the identified tows overlayed over the original image; (c) the final material map.

In the next and final step, the full map of the two material orientations is constructed by building rectangles around the tow centers (Figure 24b), each encompassing the portion of material that belongs to a tow. The dimensions of these rectangles are calculated from the optimized grid spacing. An example of the resulting material map is plotted in Figure 24c.

In conclusion, it should be remarked that this process is almost entirely automated. As pointed out in the description, only two operator interventions are required: elimination of edge cluster centroids, and selection of centroids for estimation of grid spacing.

3.3 The finite element model

A description of the finite element model of the tensile specimen will be given in this section. The model is built for finite element solver LS-Dyna Implicit, using scripts in MATLAB and Python programming languages, as well as the open-source mesh-generating software GMSH v.4.8.4.

The structured FEM mesh (Figure 25) is initially generated from a fully parametrized geometry in GMSH, and then translated to LS-Dyna keyword format. It is composed of a single layer of 4-node Belythscko-Tsay shell elements.

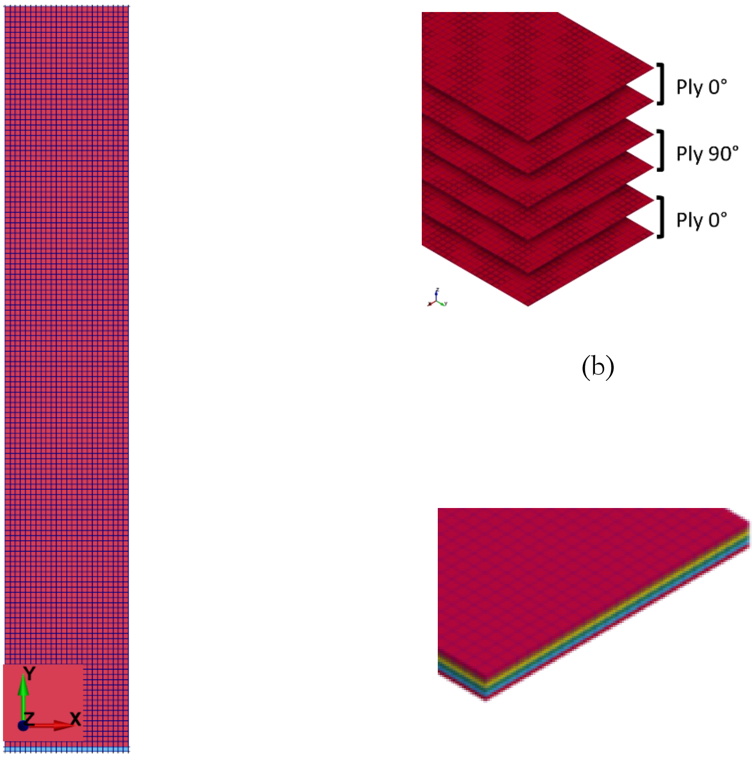

(b)

(a)

(c)

Figure 25. Finite element model of the unnotched specimen. (a) front view of the model; (b) representation showing the layers of integration points with the different materials visible, and the corresponding plies in the real material; (c) detail of the thickened shell showing the thickness of every integration point.

Six through-thickness integration points are used to represent the three composite layers, as detailed in Section 3.1, and the material is specified per every integration point. Each of the three plies in the real composite is modeled via two through-thickness integration points in the shells (Figure 25b), with alternating materials, representing the interwoven tows of fibers in a simplified fashion. A mesh convergence study was conducted to identify the appropriate mesh size, leading to a mesh size of 0.5 mm. Thus, every rectangular tow in the woven texture is represented by 10 × 20 elements.

In the testing machine, the specimen is gripped at the upper and lower ends by hydraulic grips, with the lower one being mobile. In the model, the load is introduced as a rigid body load via a row of rigid shell elements (light blue in Figure 25a) which share nodes with the lower end of the specimen. The gripping of the specimen in the testing machine is replicated via a fully constrained boundary condition on its uppermost row of nodes, and by constraining all DOFs except for displacement in Y direction on the rigid elements. In the material property identification process, the specimen is loaded by imposing the same linear load curve recorded in the experimental test.

The material model used is an orthotropic linear elastic one expressly developed for composite materials, **MAT_54* (*MAT_ENHANCED_COMPOSITE_DAMAGE*) from the LS-Dyna material library. Table 3 shows the first two cards of the material, which contain the relevant elastic parameters, and the corresponding symbols used in this work.

Table 3. Material cards 1 and 2 of LS-Dyna material **MAT_54* [68].

MID	RO	EA	EB	(EC)	PRBA	(PRCA)	(PRCB)
Material ID	Mass density	Young's modulus – long. direction $\boldsymbol{E_1}$	Young's modulus – transv. direction $\boldsymbol{E_2}$	Young's modulus – normal direction	Poisson's ratio – *ba*-direction $\boldsymbol{\nu_{12}}$	—	—

GAB	GBC	GCA	(KF)	AOPT	2WAY	TI	—
Shear modulus – *ab*-direction $\boldsymbol{G}$	—	—	—	—	—	—	—

At this stage the FEM mesh has no material orientation specified. A Python "mapping" script is used to assign the appropriate material direction to each integration point according to the map described in Section 3.2. This script parses all the (non-rigid) shell elements, computes their centroid in in-specimen coordinates, and assigns to each integration point the material orientation found in that location on the material map. The material properties themselves were identified with an optimization process, described in detail in the following section.

It is worth noting that, as for the material mapping algorithm, the construction of the FE model is almost entirely automated via Python and MATLAB scripts.

3.4 FEMU optimization of mechanical properties

3.4.1 The material property optimization algorithm

A flowchart of the optimization algorithm for data-driven identification of the elastic material properties is shown in Figure 26.

The objective is to identify the material parameters by minimizing the difference between the strains measured with DIC on the specimen surface and the corresponding strains in the FE model, i.e. the ones computed in the topmost integration points of all elements.

The algorithm is implemented in MATLAB R2021b and uses several Python scripts to interface with the LS-Dyna solver and FE results. At the center of the algorithm is a surrogate optimization solver from the MATLAB global optimization toolbox, *surrogateopt*, which was selected for its ability to converge to a global minimum and suitability for problems with objective functions that are time-consuming to evaluate [69].

The material parameters to be optimized are stored in a vector p:

$$p = [E_1, E_2, G, \upsilon_{12}], \tag{2}$$

where the symbols correspond to the ones listed in Table 3.

The optimization algorithm takes as input data the three DIC-measured strain fields on the specimen surface, the material map constructed as illustrated in Section 3.2, and the raw FEM mesh described in Section 3.3. The DIC-measured strain fields are respectively the transverse (ε_{xx}_DIC), longitudinal (ε_{yy}_DIC), and shear (ε_{xy}_DIC) strains, obtained in the post-processing detailed in Section 2.2.3 and exported to MATLAB format. In order to make them comparable, DIC and FEM strains are linearly interpolated over a common grid of points, with a spacing comparable to that of the DIC subsets. Exit conditions, an initial guess for the optimized variables p_0, as well as lower and upper bounds are also required by the optimization algorithm.

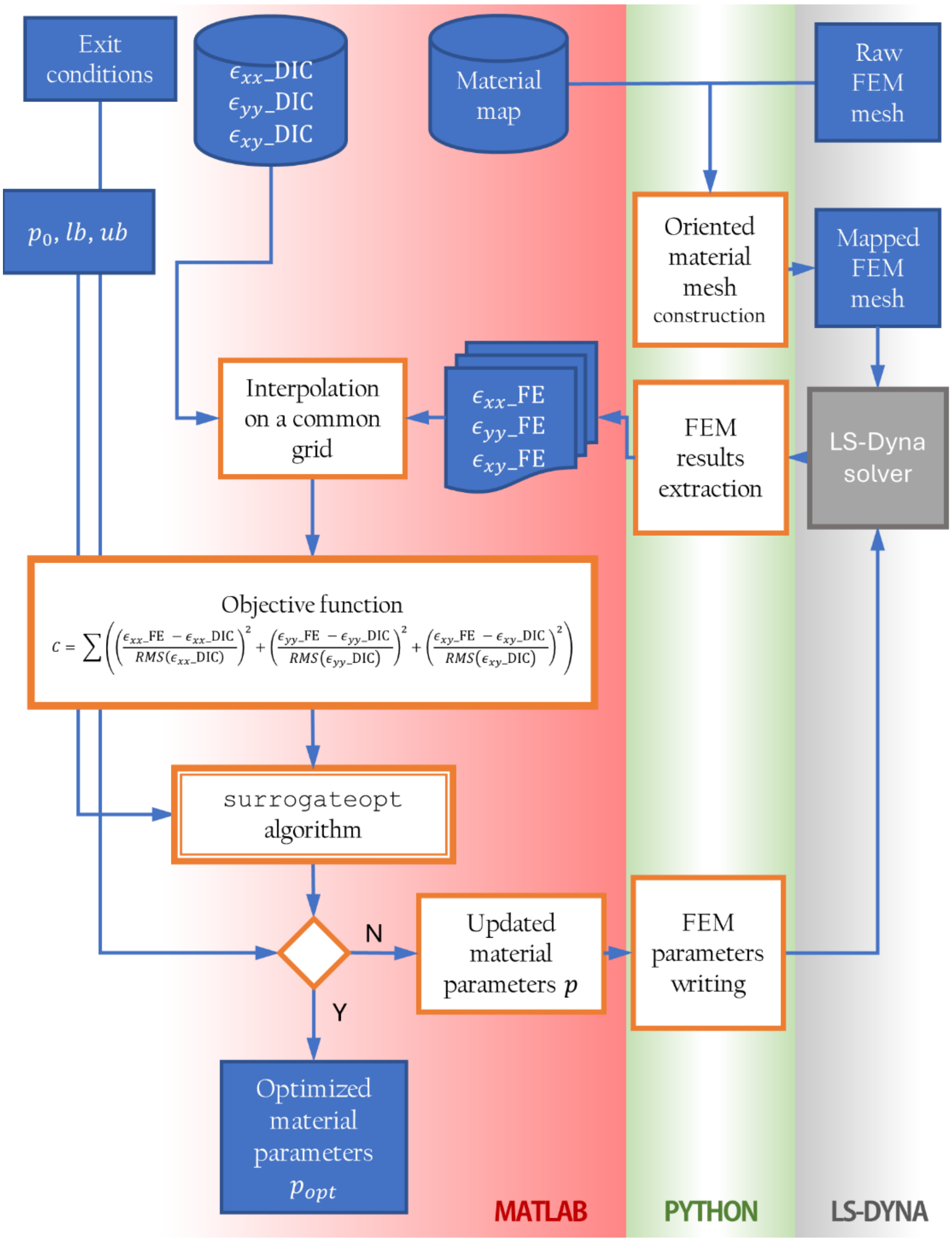

Figure 26. Flowchart of the optimization algorithm for reverse identification of the material properties.

First, the Python mapping script constructs the oriented material model, by defining according to the material map the material orientation in every integration point of every element. The LS-Dyna solver is then run. Results are extracted to MATLAB via a Python script, which makes use of the open-source *lasso-python* library [70]. The resulting FE-calculated and DIC-measured strain fields are then interpolated on the common grid.

The objective function to be minimized by the optimization algorithm can then be calculated. The function consists of the summation over the full grid of point-by-point quadratic differences between the three experimental and calculated longitudinal, transverse, and shear strain fields. Since the loading is unidirectional, the amplitude strains in the loading direction were an order of magnitude greater than those in the transverse direction. To give all the strain fields equal weight the strain field differences were normalized over their respective experimental RMS values. Mathematically, the objective function C is therefore formulated as:

$$C = \sum \left(\left(\frac{\varepsilon_{xx}^{FE} - \varepsilon_{xx}^{DIC}}{RMS(\varepsilon_{xx}^{DIC})} \right)^2 + \left(\frac{\varepsilon_{yy}^{FE} - \varepsilon_{yy}^{DIC}}{RMS(\varepsilon_{yy}^{DIC})} \right)^2 + \left(\frac{\varepsilon_{xy}^{FE} - \varepsilon_{xy}^{DIC}}{RMS(\varepsilon_{xy}^{DIC})} \right)^2 \right), \tag{3}$$

where ε_{xx}, ε_{yy}, and ε_{xy}, are the transverse, longitudinal, and plane shear strain fields, respectively, the ^{FE} and ^{DIC} superscripts indicate numerical and experimental DIC grid-interpolated strain fields, $RMS(\varepsilon)$ is the root mean square of the strain field ε; and Σ is the summation over all the common strain field grid points. Based on the value of the objective function, the surrogate optimization algorithm determines the next value of p, which is written in the FE model and a new iteration begins. The output of the algorithm is a vector of optimized properties p_{opt}.

3.5 Optimized material properties

The elastic material properties resulting from the optimization process are reported in Table 4. These same values will be used in the finite element simulations in the remainder of this work. A comparison of the experimental and numerical longitudinal strain fields after optimization is shown in Figure 27. It can be appreciated how the model captures well the diagonal strain banding typical of woven twill composites.

Table 4. Elastic material properties obtained from the optimization algorithm.

Property	E_1 [GPa]	E_2 [GPa]	G_{12} [GPa]	υ_{12}
Value	102.388	15.519	1.891	0.050

A brief discussion of the properties is given here. It is interesting to note how the average of longitudinal and transverse moduli E_1 and E_2, $\bar{E} = 58.95\ GPa$, is close to the value of the modulus of the homogenized material $E = 54.34\ GPa$ (Table 2). Effective separation of the horizontal and vertical tows in the material mapping stage was found to be critical to good mesoscale elastic parameter calibration. Failure to achieve this separation resulted in the longitudinal and transverse elastic moduli converging toward this average value.

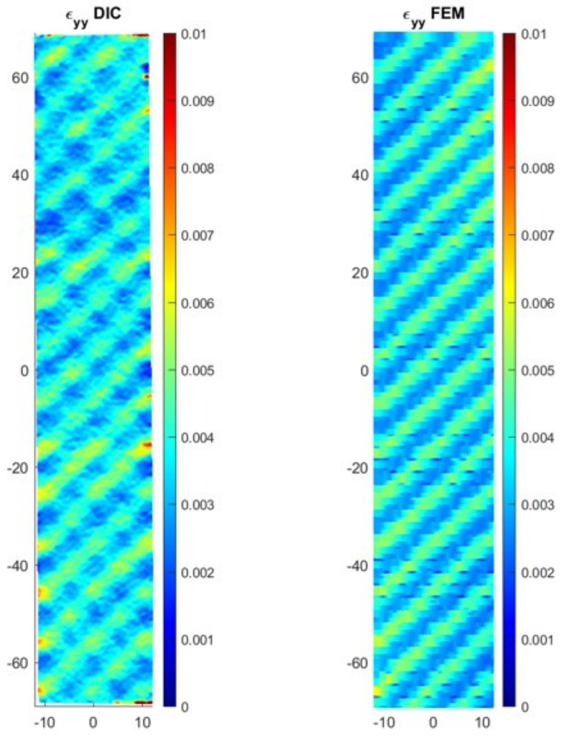

(a) (b)

Figure 27. Longitudinal strain fields in unnotched specimen C20_4: (a) experimental, (b) numerical, after parameter optimization.

The operation of mapping the material orientation is equivalent to reducing it to a unidirectional composite (the individual fiber tows) from which it is constituted. The transverse elastic modulus E_2 obtained is comparable to the typical one for such a material, however the longitudinal modulus E_1 is somewhat lower than usual. This discrepancy can be attributed to the formulation of the finite element model. Fiber bundles are not entirely planar, but rather curve in the through-thickness direction due to the woven structure of the composite. This results in a local change of the elastic property along the bundle itself, according to the curvature of the bundle: in the in-plane direction, the stiffness of the bundle decreases. In the finite element model all elements in the fiber tow have the same properties, and this geometrical change in elastic properties does not take place. It is therefore reflected in lower longitudinal elastic properties than those typical of unidirectional carbon fiber composite. Tow curvature, however, does not influence the elastic properties of the transverse tows. The value of the transverse modulus obtained therefore aligns with that typical of unidirectional composite.

In the following chapter, the material properties thus obtained will be used to model tensile tests on open-hole specimens.

Chapter 4

Numerical modeling and stress analysis

This chapter presents the results of the simulation of all open-hole tensile tests with calibrated mesoscale FE models.

Section 4.1 contains a discussion of the simulation and results. In Section 4.2 the stress fields thus obtained are used to analyze at the mesoscale the effect of width/diameter scaling.

4.1 Simulation of the open-hole tensile tests

4.1.1 The numerical model

The finite element model of each tested specimen was constructed with a procedure similar to that of the material property identification model, i.e. with a material map obtained with the automated procedure from Section 3.2 applied to the FE model from Section 3.3. Therefore, in this section only the points of difference with the previously described model will be discussed.

Since a quantity of tests on similar specimen geometries had to be simulated, a Python script was used to automatically generate FE models from basic LS-Dyna files, ready to be solved and complete with the desired geometrical dimensions, mesh size, material orientation distribution, loading data, and material parameters. Figure 28a shows the geometry which underpinned the structured mesh of every specimen, parametrized and constructed in GMSH. The same base geometry was used for all six types of specimens, by changing dimensional parameters. The meshed geometry for a C22 specimen is visible in Figure 28b. Base mesh size away from the hole was 0.5 mm, in order to have 10 × 20 elements for each tow of the woven twill texture. The structured mesh was refined around the hole, with a minimum size of 0.05 mm—constant for all specimen types.

The material properties used in the models were those determined with the optimization process detailed in Chapter 3 and reported in Table 4. As in the FEMU process, the model was loaded with the experimentally recorded load curve. Experimental loads and displacements at failure recorded for each specimen tested are reported in Table 5.

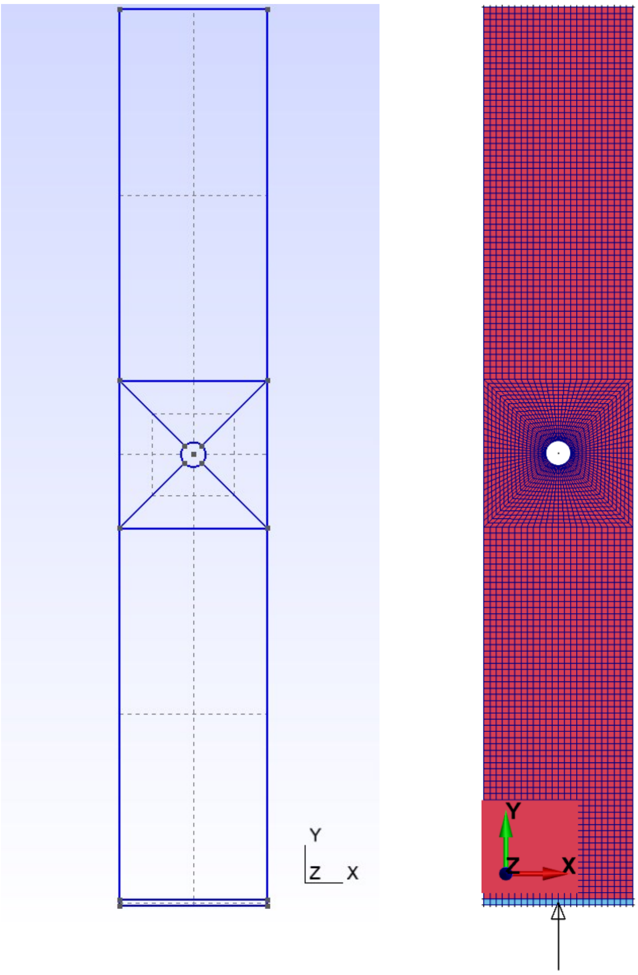

(a) (b)

Figure 28. FEM model of the open-hole specimens: (a) parametrized geometry, (b) meshed model.

4.1.2 Results of numerical modeling

The last two columns of Table 5 list the displacement at failure in the numerical model and its percentage error with the experimental measurement. The error was computed as the difference between the experimental and numerical displacements, normalized over the experimental displacement. The results show an average absolute error of 3.81% and a standard deviation of 3.03%.

Table 5. Experimental failure load, experimental failure displacement, FEM failure displacement, and the percentage error between the last two for each specimen.

Specimen	$P_{exp,\,max}$ [kN]	d_{exp} [mm]	d_{FEM} [mm]	d err%
C21_1	30.929	-1.631	-1.616	0.96%
C21_2	30.976	-1.663	-1.622	2.49%
C21_3	30.778	-1.656	-1.608	2.92%
C22_1	26.811	-1.528	-1.430	6.44%
C22_2	25.768	-1.427	-1.374	3.71%
C22_3	25.768	-1.461	-1.372	6.04%
C23_1	20.957	-1.385	-1.209	12.69%
C23_2	20.749	-1.276	-1.200	5.96%
C23_3	22.075	-1.366	-1.277	6.47%
C31_1	48.570	-1.654	-1.701	-2.85%
C31_2	50.791	-1.740	-1.778	-2.17%
C31_3	47.376	-1.593	-1.657	-4.01%
C32_1	39.633	-1.424	-1.428	-0.25%
C32_2	37.551	-1.357	-1.353	0.35%
C32_3	41.111	-1.452	-1.481	-2.00%
C33_1	32.262	-1.380	-1.303	5.54%
C33_2	31.440	-1.302	-1.270	2.41%
C33_3	31.150	-1.286	-1.270	1.25%

In Figure 30 the load and displacement curves from all the simulated tensile tests are compared with the experimental ones. The same is done in Figure 31 for the stress and strain curves. Here the experimental strain is the average over the entire DIC AOI, while the numerical one is the average over the topmost integration point, corresponding to the surface of the specimen. Stresses are calculated as engineering stresses on the gross unnotched cross-section.

The mesoscale finite element model captures accurately the global elastic behavior of the tested specimens, thus validating the material properties obtained separately via calibration from an unnotched specimen. This can also be appreciated on a mesoscopic level as shown in Figure 29, through the comparative analysis of the strain fields in the longitudinal direction. The model reproduces to a good degree the surface strain variations due to the material heterogeneity and its interaction with the strain intensification in the vicinity of the circular notch. The diagonal banding effect in the strain field stemming from the twill structure is also well represented, as is the secondary opposite direction diagonal banding due to the 90° middle ply.

The slightly nonlinear trend of the experimental stress-strain curves in the proximity of the final failure results in a minor discrepancy to the finite element model. The FE model indeed did not contain a damage law and assumed an elastic behavior until the final failure, for the sake of simplicity.

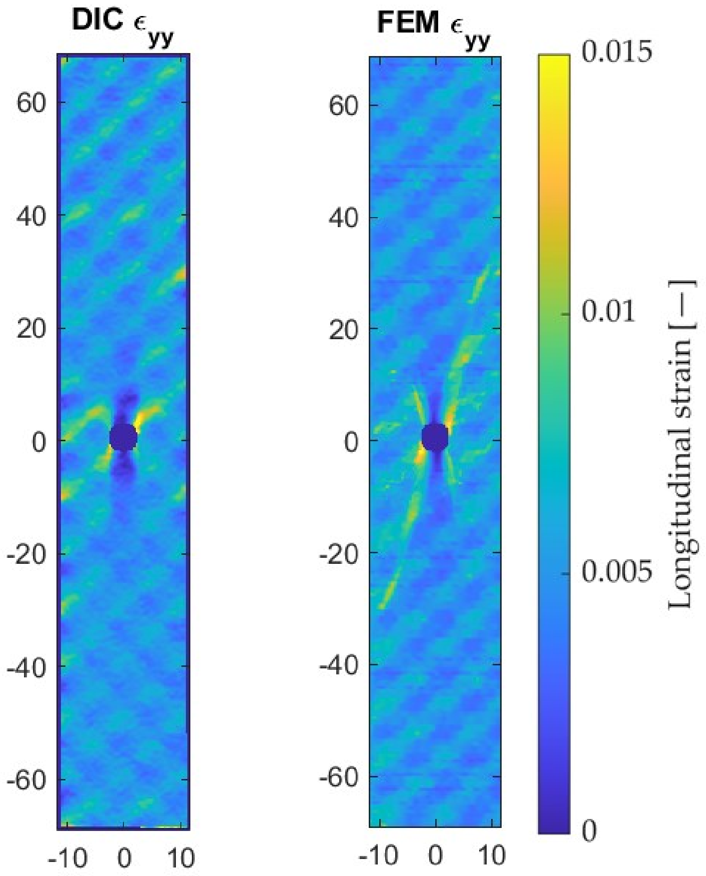

Figure 29. Example of a comparison (specifically, for Specimen C22_2) between experimentally and numerically determined longitudinal strain maps.

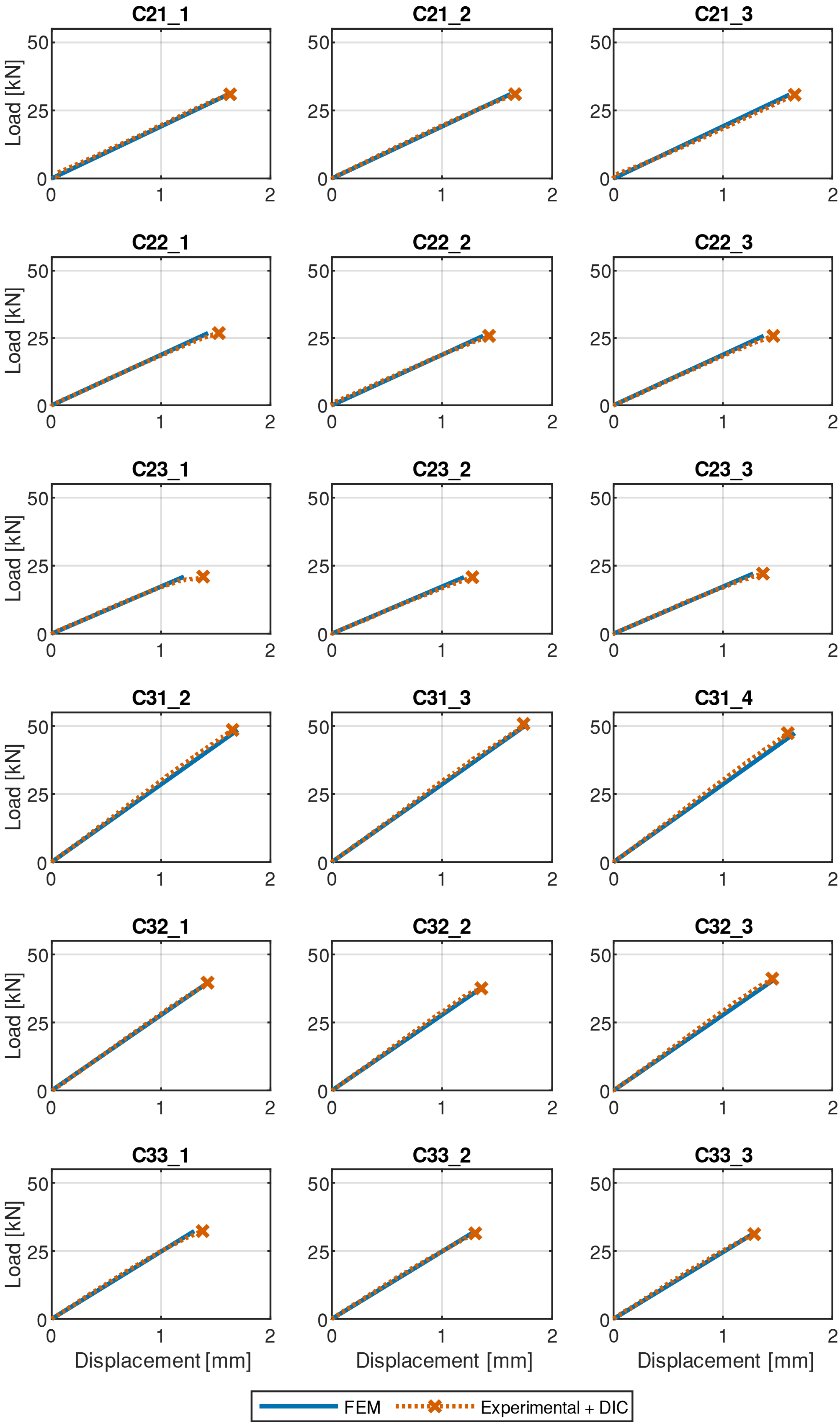

Figure 30. Comparison of experimental and numerical load-displacement curves for all the specimens tested.

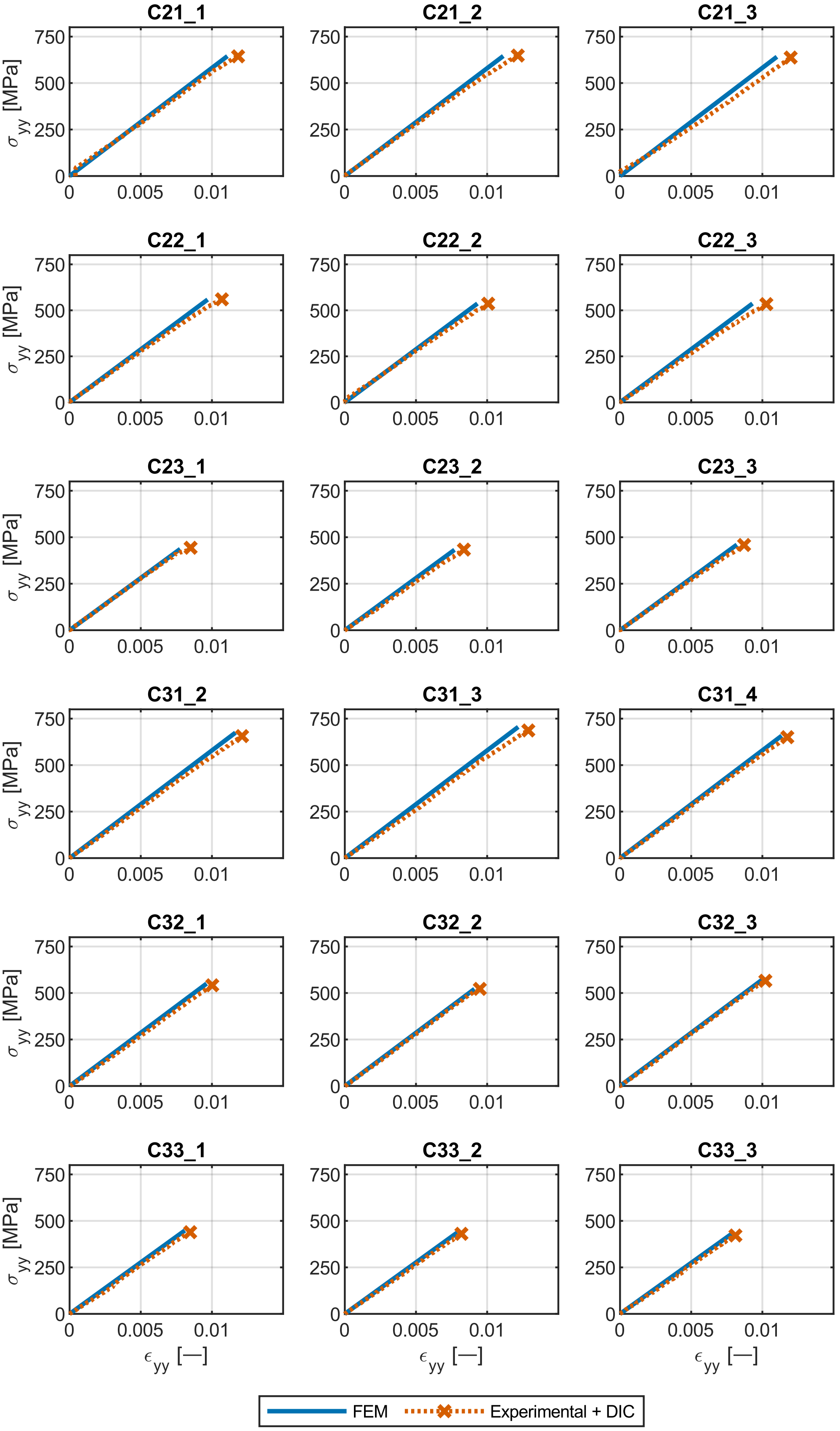

Figure 31. Comparison of experimental and numerical average longitudinal stress-strain curves for all the specimens tested.

4.2 Reinterpretation of stress concentration

A mesoscale analysis of stress concentration on a subset of the tested specimens is presented in this section. In particular, the FEM stress fields at failure in representatives of each of the six specimen types were considered.

4.2.1 Failure properties

The analysis focused on failure stresses in the specimens at failure. For each individual specimen, these were extracted from the FEM stresses at a loading state corresponding to the experimental failure one.

It should be noted that in the following, consistently with the diagram in Figure 18c on page 28, x and y denote the global directions, with y being the longitudinal, tensile loading one; while 1 and 2 are the local material directions in each unidirectional fiber tow, with 1 being the fiber direction, and 2 the matrix direction.

The base material properties were extracted from a *C20* plain specimen. Failure was modeled with the Hashin criterion, which is implemented in the material model selected, **MAT_54* of LS-Dyna. The choice of this criterion is consistent with each tow being a unidirectional fiber composite. Several hypotheses on failure were made, based on the particular unidirectional loading condition and the nature of the composite's constituent material:

1. The stresses responsible for failure are longitudinal stress σ_{yy} and shear stress τ_{xy};
2. In vertically oriented tows, aligned with the loading direction, the main tensile stresses σ_{yy} are in the longitudinal ("fiber") direction of the material. Failure is due to fiber breakage. The corresponding failure criterion is:

$$e_f^2 = \left(\frac{\sigma_{yy}}{S_1}\right)^2 - 1 \qquad e_f^2 \geq 0 \Leftrightarrow \text{failure}, \tag{4}$$

   where σ_{yy} is the longitudinal stress, S_1 represents the longitudinal tensile strength of the tow material, and e_f is the failure index in the fiber direction.

3. In horizontally oriented tows, the main tensile stresses σ_{yy} are in the transverse ("matrix") direction of the material. Failure is due to matrix failure caused by tensile stresses combined with shear stresses. The failure criterion is:

$$e_m^2 = \left(\frac{\sigma_{yy}}{S_2}\right)^2 + \left(\frac{\tau_{xy}}{S_{12}}\right)^2 - 1 \qquad e_m^2 \geq 0 \Leftrightarrow \text{failure}, \tag{5}$$

where σ_{yy} and τ_{xy} denote longitudinal and shear stresses, S_2 is the transverse tensile strength of the tow material, S_{12} is the shear strength of the tow material, and e_m is the failure index in the matrix direction.

The three material strength parameters, S_1, S_2, and S_{12}, were evaluated by analyzing the maximum stress state in the numerical model, on a ply-by-ply basis.

The stress state of notched specimens was studied with a similar approach. From the validated mesoscale FEM, the stress concentration, the location of the most severely loaded elements, and the volume of material affected by stress concentration were recovered. This information was used to investigate the size effect due to stress concentration.

The failure strengths identified for the constituent material following the procedure described are summed up in Table 6.

Table 6. Failure properties for each specimen considered.

Specimen	S_1 [MPa]	S_2 [MPa]	S_{12} [MPa]
C20	2131	370	117
C21	3680	625	123
C22	3646	584	162
C23	3906	623	187
C31	4223	702	163
C32	4119	668	197
C33	4512	758	217

In line with the hypotheses on failure, the maximum longitudinal stress always occurred in elements within longitudinal (vertical) tows, whereas maximum transverse and shear stresses were always in horizontal tows.

4.2.2 Volumes affected by the concentration

To assess the level of stress intensification, the volume of material affected by the notch was calculated. The definition of this volume is the sum of the volumes of material belonging to integration points where stress at failure surpassed the remote stresses in the specimen. These remote stresses (σ_1^∞ and σ_2^∞, with subscripts specifying the local material direction) were defined in turn as the maximum stresses observed in regions of the specimen away from both the fixture and the stress concentration areas, spanning the width of the specimen and multiples in size of the characteristic dimension of the tows. Affected volumes were considered separately for vertical and horizontal tows. Figure 32 shows a mapping of the percentage of the volume of every element affected by the stress concentration, for the notched specimens included in the analysis. Table 7 collects the values calculated for each notched specimen. Here “Volume 1” and “Volume 2” indicate the volume undergoing stress concentration along material directions 1 and 2.

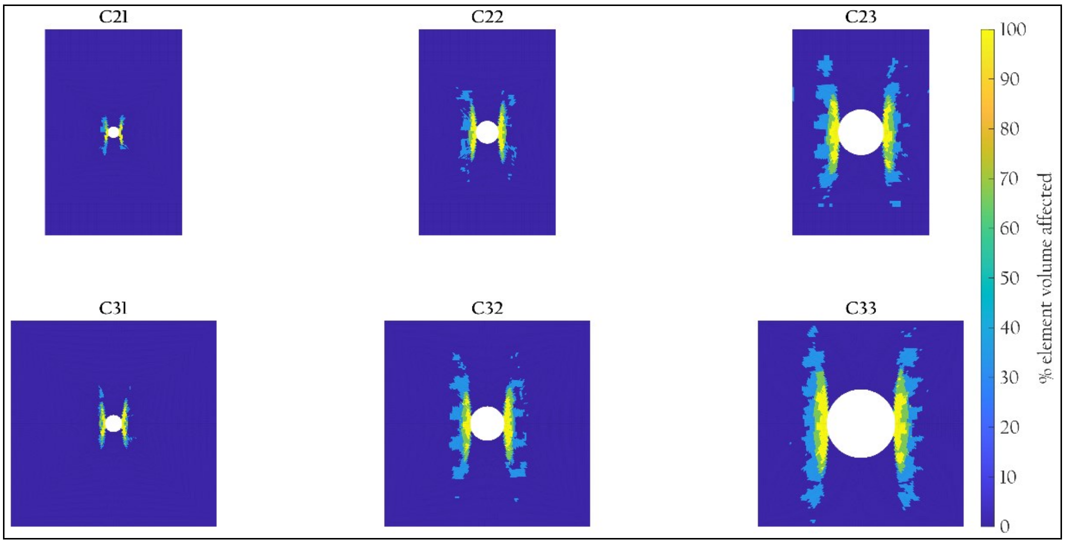

(a)

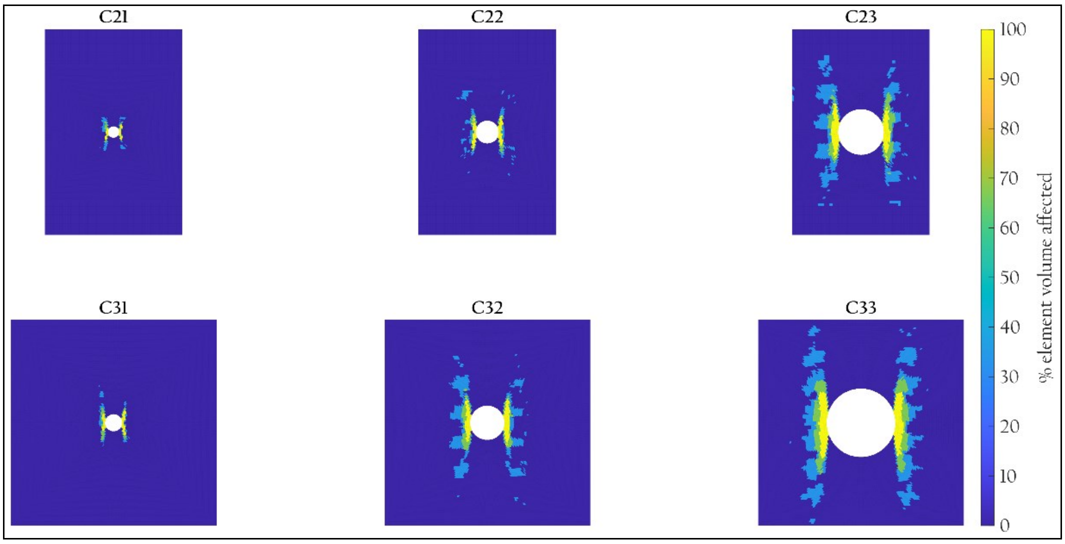

(b)

Figure 32. Maps of the volume of material affected by stress concentration, in (a) vertical and (b) horizontal tows, in the considered specimens.

Table 7. Volumes affected by the stress concentration, in vertical tows and horizontal tows.

Specimen	Volume 1 [mm^3]	Volume 2 [mm^3]	Total volume [mm^3]
C21	5.04	3.77	8.80
C22	22.15	11.39	33.55
C23	58.83	47.13	105.96
C31	10.21	6.74	16.95
C32	44.00	33.01	77.01
C33	93.60	82.15	175.75

The scaling of the affected volume with the hole diameter can be observed. It is also possible to examine the interaction of the stress concentration with the heterogeneous material. The stress concentration is more localized in the specimens C21, C31, and C22, where at 2 mm, 3 mm, and 4 mm diameter respectively, the notches are smaller than the 5 mm tow size. Conversely in specimen C31, C23, and C33, where the hole diameter is larger than the tow size, the notch extends across multiple tows and breaks up more than one diagonal row of tows. Bundles of vertical fibers completely interrupted by the notch are unloaded; instead, load has to be transferred by shear stresses to the tows on either side of the notch. This less effective use of the material causes a broader distribution of affected volume.

4.2.3 Stress ratios

A separate analysis may be conducted on the individual highest stressed elements, rather than on all the affected ones. In Figure 33 the highest stress integration points are plotted on the σ_{yy}–τ_{xy} plane (fiber direction in the material) and σ_{xx}–τ_{xy} plane (matrix direction in the material), for the three 24 mm specimens considered (Figure 33a) and the three 36 mm ones (Figure 33b). All stress states of the elements in the unnotched specimen at failure are also plotted as a point cloud in grey.

There is a clear distinction in the stress states found in the vertical and the horizontal tows. The former carry the highest fiber-direction tensile stresses, and the latter the highest matrix tensile and shear stresses. It is worth pointing out how every single element in the unnotched specimen is at significantly lower stress levels, in spite of its apparent higher ultimate tensile strength.

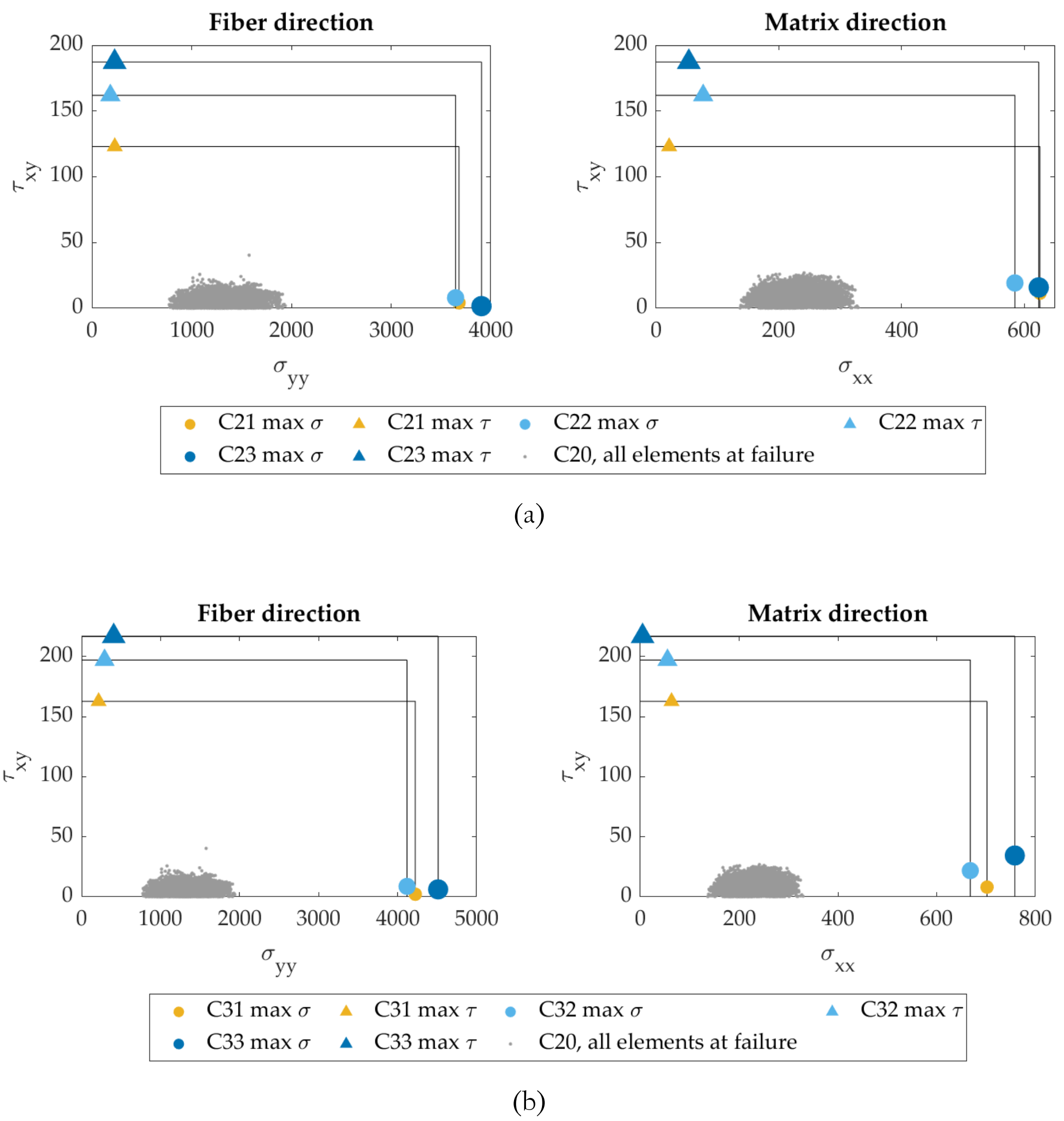

(a)

(b)

Figure 33. The stress states of the most heavily loaded elements at failure, plotted on the σ_{yy}–τ_{xy} plane, and on the σ_{xx}–τ_{xy} plane. (a) 24 mm specimens, (b) 36 mm specimens. The grey point cloud contains all stress states in the unnotched *C20* specimen.

What can be garnered from these two analyses is that the circular hole causes in the stress field two distinct effects:

1. Stress concentration. The volume affected by the notch scales up with its diameter. As a result of this, there is an increased probability of a finding defect large enough to cause failure, which decreases the load-bearing ability. As a matter of fact, the nominal strength of the notched specimen, defined as the ratio between maximum load and the nominal notched cross-section, decreases with increasing hole diameters. It is possible to gauge this effect by comparing the remote longitudinal stress σ_1^{∞}, as detailed earlier, with the maximum longitudinal stress in the whole specimen σ_1^{MAX}.

This results in the non-dimensional stress ratio $\sigma_{1\,ratio}$:

$$\sigma_{1\,ratio} = \frac{\sigma_1^{\infty}}{\sigma_1^{MAX}}. \tag{6}$$

2. Stress localization. In the vicinity of the notch, there is a sharp rise in stress in a limited volume, leading to an observed localized material strength increment. This effect can be quantified by the ratio of the longitudinal tensile strength of the material in the notched specimens S_1 to the corresponding property in the unnotched specimen, denoted as S_1^0. This results in the non-dimensional stress ratio $\mathrm{S}_{1\,ratio}$:

$$S_{1\,ratio} = \frac{S_1}{S_1^0}. \tag{7}$$

For clarity, the origin of these stresses combined into these two ratios is represented in Figure 34. The reference unnotched specimen is to the left, and a notched specimen is to the right.

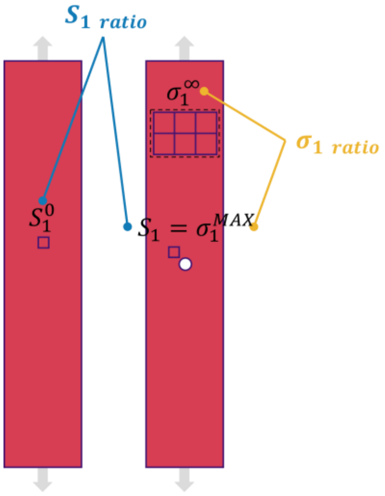

Figure 34. Computation of the stress ratios $\sigma_{1\,ratio}$ and $S_{1\,ratio}$.

At specimen level, the global tensile behavior is the result of a superposition of these two effects, one adding and the other detracting from mechanical strength. To highlight this, the non-dimensional stress ratios describing the two effects are plotted in Figure 35a with different hole diameters highlighted. Here the same quantities are represented by the same color, while line type indicates the specimen width—solid for 24 mm and dotted for 36 mm. The yellow curves, $\sigma_{1\,ratio}$, characterize the stress concentration. For increasing hole diameter there is a decrease in the ratio between the remote stress and maximum stress, induced by an intensification of the stress and a larger affected area.

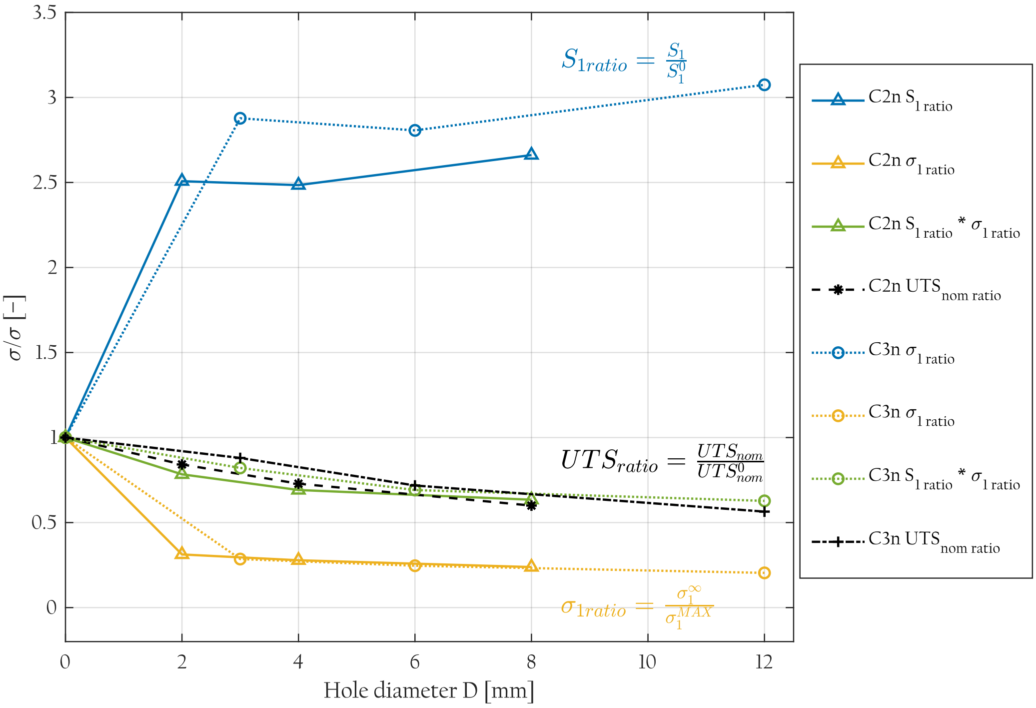

Figure 35. The two mesoscale effects on stress ratios plotted for increasing hole diameters, for both specimen groups: 24 mm specimens with solid lines, and 36 mm ones with dotted lines.

The ratios between the notched and unnotched tensile strength of the material $S_{1\,ratio}$ are plotted in blue. A roughly 2.5-fold increase in the local strength of the tow material in 24 mm specimens, rising to 2.9 for 36 mm ones. The local strength increases in parallel with the hole diameter.

The two effects can be combined by dividing the strength increase by the stress intensification, as depicted by the green curves. The latter follow closely the black dashed lines, representing the reduction in nominal ultimate tensile strength UTS_{nom} compared to the unnotched value UTS_{nom}^0:

$$UTS_{ratio} = \frac{UTS_{nom}}{UTS_{nom}^0}. \tag{8}$$

This ultimate tensile strength ratio is the quantity typically used in specimen-level analysis of open-hole stress concentration. An interpretation of the good agreement of the respective $S_1 * \sigma_{1\,ratio}$ and UTS_{nom} curves for the two width groups of specimens, is a correspondence between a mesoscale-level and a macroscale-level stress concentration curve.

With increasing notch diameters there is an observable decrease in slope in the nominal stress curve. Knowing the two effects described previously, this change in slope may be now interpreted as a change in their relative weight, which occurs with hole size scaling. For a growing hole diameter, the decrement of local material strength caused by to the larger affected area is outweighed by the parallel increment due to stress localization.

Chapter 5

Statistical modeling of open-hole tensile strength

This chapter describes how the strength of a single tow has been studied through a statistical approach, leveraging the knowledge of stress states in the woven composite specimens obtained from the mesoscale finite element models.

Section 5.1 deals with the derivation of the statistical model, while Section 5.2 details the optimization strategy for the identification of its parameters. Finally, Section 5.3 presents the results of the statistical model.

5.1 Derivation of the statistical model

The component of total volume V, in this case the open-hole tensile specimen, can be subdivided into n elementary elements (Figure 36). The i-th element is characterized by a volume v_i and a characteristic strength $\sigma_{f,i}$, and is undergoing a stress state σ_i.

It is assumed that the strength of the element, whose constituent material is a brittle, high-modulus fiber unidirectional composite, follows a Weibull distribution:

$$\sigma_{f,i} \approx weib(\eta_i, \beta), \tag{9}$$

where η_i is the size parameter, related to the characteristic strength per unit volume, and β the shape parameter, associated with material strength variability.

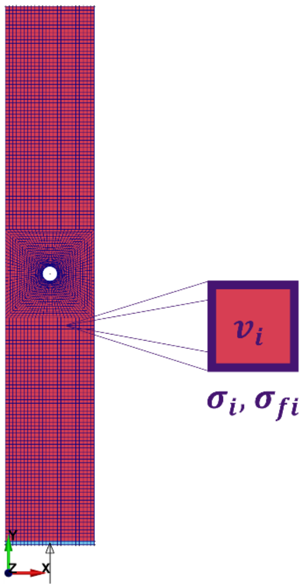

Figure 36. Discretization of the specimen in elementary volumes.

5.1.1 The equivalent stress

As assessed in the previous chapter, the stress state in the twill composite material studied during open-hole tensile testing is complex, due to the stress concentration induced by the presence of the notch, further altered by the heterogeneous material distribution. In order to appropriately take this into consideration while simultaneously reducing the problem dimensionality to fit the statistical model, an equivalent stress was introduced for the orthotropic material which represents the single tow.

The formulation of the equivalent stress is analogous to the Tsai–Hill failure criterion. Like this criterion, it comprises four quadratic terms, accounting for longitudinal (fiber direction) tensile stress, transverse (matrix direction) tensile stress, their interaction, and shear stress. The definition of the equivalent stress σ_{eq} for the i-th element is therefore the following:

$$\sigma_{eq,i}^2 = \varphi_1^2\, \sigma_{1,i}^2 + \varphi_2^2\, \sigma_{2,i}^2 + \varphi_3^2\, \sigma_{1,i}\, \sigma_{2,i} + \varphi_4^2\, \sigma_{12,i}^2\,, \tag{10}$$

where $\sigma_{1,i}$, $\sigma_{2,i}$, and $\sigma_{12,i}$ are, respectively, the fiber-direction tensile, transverse tensile, and shear stress in the i-th element; while $\varphi_1, \varphi_2, \varphi_3$, and φ_4 are parameters to be estimated from experimental results, which are related to the material strength.

In the rest of this chapter, the scale effect that determines the variation of the material strength with the critical volume (which is, the volume experiencing critical stress) will be modeled by expressing statistically the limit value of the equivalent stress of the tow material.

5.1.2 The statistical size effect

To model the relationship that links critical volumes and material strength it is necessary to know the stress field in the structure object of study. Given that the dimensions of the notch and fiber tows are comparable, the size effect is modeled at the mesoscale level. This requires determining the stress field and the critical volume at mesoscale using the FE model described in Chapter 3 and applied to all tested specimens in Chapter 4.

The approach introduced here adapts the statistical methodology presented in [50], originally developed for modeling the size effect in the fatigue behavior of components. As prefaced, the random variable is the maximum equivalent stress in the component $\sigma_{eq,max}$. The volume of the part—here, the open-hole tensile specimen—is discretized through a linear elastic finite element model in sub-volumes, each characterized by an equivalent stress, $\sigma_{eq,i}$. The failure probability of the sub-volume scales with the equivalent stress. Additionally, in accordance with the weakest-link principle, the larger a sub-volume with a specific equivalent stress is, the higher the probability of failure. Assuming the equivalent failure stress, $\sigma_{f,i}$, of an individual element follows a Weibull distribution [1], the reliability of a single element is given by:

$$R_{\sigma_{f,i}}(\sigma_{eq,i}) = exp\left[-\left(\frac{\sigma_{eq,i}}{\eta_i}\right)^{\beta}\right], \tag{11}$$

where β and η_i represent respectively the shape and scale parameters of the Weibull distribution. The relationship between the element reliability and its volume, v_i, is modeled by the following expression:

$$\eta_i = \alpha \, (v_i)^{\gamma} \, , \tag{12}$$

where α and γ are two parameters that must be estimated from experimental data.

Taking now into consideration a part or component, such as the open-hole specimen, composed of n elements, its reliability R_{part} following the weakest-link principle is:

$$\begin{aligned} R_{part} = {} & P\left[\left(\sigma_{f,1} > \sigma_{eq,1}\right) and \ldots \left(\sigma_{f,i} > \sigma_{eq,i}\right) and \ldots \left(\sigma_{f,n} > \sigma_{eq,n}\right)\right] = \\ & = P\left[\sigma_{f,1} > \sigma_{eq,1}\right] \cdot \ldots \cdot P\left[\sigma_{f,i} > \sigma_{eq,i}\right] \cdot \ldots \cdot P\left[\sigma_{f,n} > \sigma_{eq,n}\right] = \\ & = \prod_{i=1}^{n_{el}} R_{\sigma_{f,i}}(\sigma_{eq,i}) \, . \end{aligned} \tag{13}$$

In the following the ratio of each element's equivalent stress, $\sigma_{eq,i}$, to the maximum in the entire component, $\sigma_{eq,max}$, will be denoted as:

$$\sigma_{eq,ratio,i} = \frac{\sigma_{eq,i}}{\sigma_{eq,max}}, \tag{14}$$

By substituting Equation (11) in (13), applying a logarithmic transformation, and introducing the variable $\sigma_{eq,ratio,i}$ defined in (14), the probability of failure of the part, F_{part}, can be expressed as:

$$F_{part}(\sigma_{eq,max}) = 1 - R_{part} = 1 - exp\left[-(\sigma_{eq,max})^{\beta} \sum_{i=1}^{n_{el}} \frac{(\sigma_{eq,ratio,i})^{\beta}}{\alpha\ (v_i)^{\delta}}\right]. \tag{15}$$

Here v_i and $\sigma_{eq,ratio,i}$ are, respectively, the volume and the equivalent stress ratio in the i-th out of n elements, into which the component is divided. Additionally, α, β, and $\delta = \beta \cdot \gamma$ are three parameters.

5.2 Identification of the model parameters

An optimization procedure is used to identify from the experimental data the three model parameters α, β, and δ, as well as the four φ parameters for the equivalent stress formulation. The foundation of this procedure and its practical implementation are discussed in the following two sections.

5.2.1 Principle of operation

The stress fields computed in the FEM at failure load are initially used to calculate the experimental maximum equivalent stress within every tested specimen with Equation (10). The empirical cumulative distribution function (CDF) of these observations, or F_{exp}, is estimated by applying Benard's approximation of the median rank [71]:

$$F_{exp} = \frac{i\ -\ 0.3}{N\ +\ 0.4}, \tag{16}$$

where i denotes the rank of the observation and N the total number of tests.

The model-calculated probability of failure, F_{mod}, must be as close as possible to the empirical one, F_{exp}, in order for the model to correctly represent this distribution. In an F_{exp}–F_{mod} probability–probability plot, this means that all points are situated on the bisector of the first quadrant. The statistical model parameters may therefore be identified by minimizing the following objective function:

$$R^2 = \frac{RSS}{TSS}. \tag{17}$$

Here **RSS** is the residual sum of squares and **TSS** the total sum of squares in a P-P plot, where the calculated probability of failure acts as the independent variable and the empirical probability as the dependent variable.

5.2.2 Description of the optimization algorithm

A flowchart of the algorithm for optimization of the statistical model parameters is shown in Figure 37. The algorithm was set up in MATLAB R2021b. The objective function was minimized using the MATLAB function *fminsearch*, which implements the Nelder–Mead simplex algorithm [72].

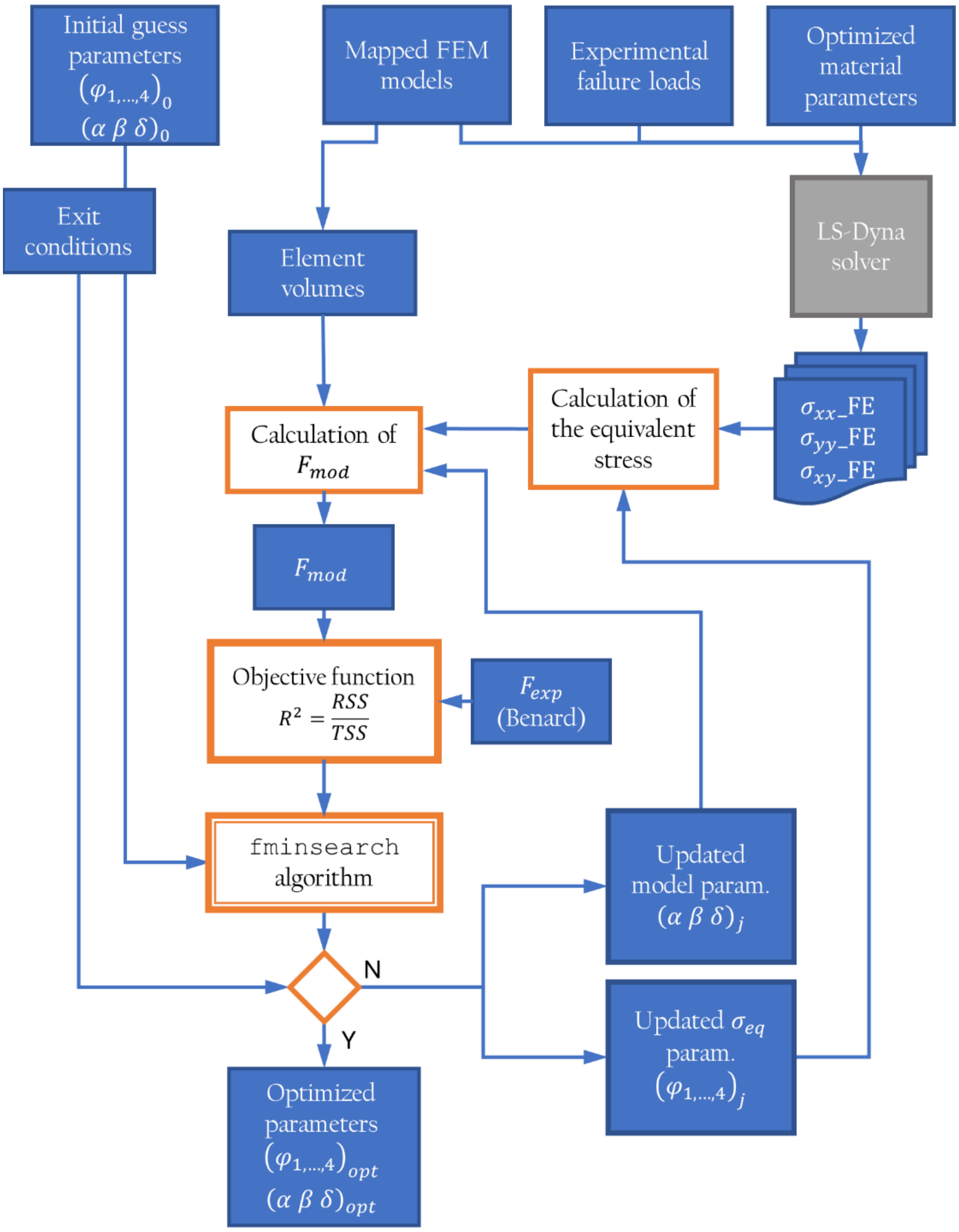

Figure 37. Flowchart of the algorithm used to identify the statistical model parameters.

The optimization algorithm requires as input the stress fields in each tested specimen. These are extracted from the results of LS-Dyna solver, which in turn takes in the optimized material parameters, experimental failure loads, and mapped FEM models described in Chapters 3 and 4. The element volumes in each specimen are also extracted from the mapped models.

A function calculates the equivalent stress in every element of each specimen according to Equation (10), from the stress fields and initial guess stress formulation parameters $(\varphi_1, \dots, \varphi_4)_0$. Equivalent stresses together with the element volumes are passed on to a second function, which calculates the model probability of failure F_{mod} according to (15).

The objective function to be minimized by the optimization algorithm can then be calculated. Based on its value, the *fminsearch* algorithm determines the next value of the parameters $(\alpha, \beta, \delta)_j$, and $(\varphi_1, \dots, \varphi_4)_j$., which are passed to the equivalent stress calculation function and the F_{mod} calculation function respectively, and a new iteration begins. Once exit conditions are met, the output are vectors of optimized parameter vectors $(\alpha, \beta, \delta)_{opt}$, and $(\varphi_1, \dots, \varphi_4)_{opt}$.

5.3 Results of the statistical model

Because only three replications per width-to-diameter ratio were available, the specimens were categorized into two groups on the basis of their width. This dimension was considered as the dominant factor affecting the scale parameter, an assumption supported by the model's findings discussed later. Therefore, two separate empirical and model-estimated statistical distributions were constructed: one for the 24 mm wide specimens, and another for the 36 mm wide specimens.

As mentioned before, the goodness of fit of the model to the empirical data may be evaluated through a probability–probability plot, which compares two cumulative distribution functions. The probability–probability plot of the model-estimated CDF (F_{mod}), after having optimized the four parameters, versus the experimental empirical CDF (F_{exp}), for the two specimen types, is shown in Figure 38.

The coefficient of determination for the statistical model predictions compared to the experimental data is $R^2 = 94\%$, as visible in Figure 38. This confirms that the calibrated model accurately captures the size effect controlling the failure of the open-hole specimens. While all data points lie close to the bisector, the model tends to slightly underestimate the probability for the wider specimens, and to overestimate it for the narrower ones.

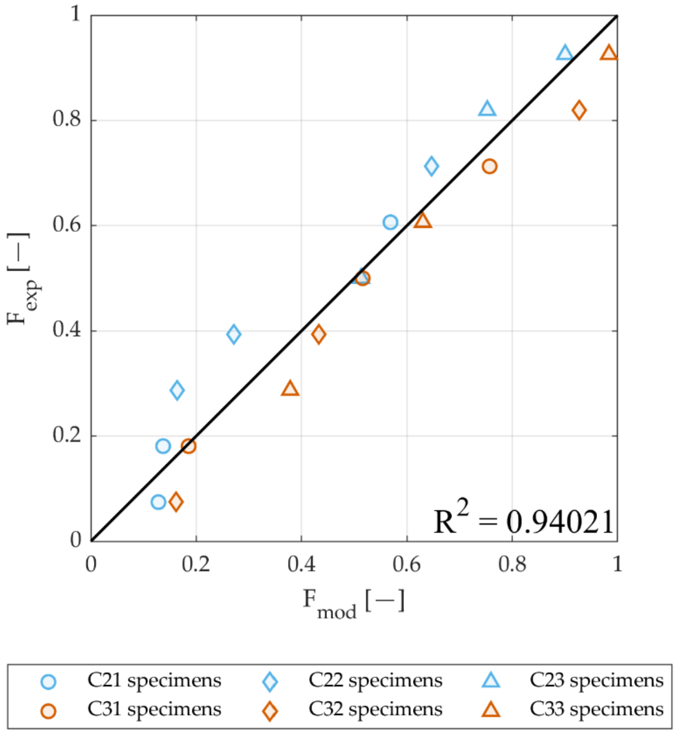

Figure 38. Probability–probability plot of the model-estimated CDF (F_{mod}) versus the experimental empirical CDF (F_{exp}) for the 36 mm wide (in orange) and 24 mm wide specimens (in blue). Also shown is the coefficient of determination, R^2, of the least squares fit of the bisector to the data points.

The model parameters determined through the optimization procedure are tabulated below: Table 8 lists the four equivalent stress parameters, and Table 9 the three statistical model parameters.

Table 8. Values of the four parameters of the equivalent stress formulation, which were estimated from the experimental data.

$\boldsymbol{\varphi_1}$	$\boldsymbol{\varphi_3}$	$\boldsymbol{\varphi_3}$	$\boldsymbol{\varphi_4}$
0.0613	0.5823	0.3033	1.1198

Table 9. Values of the three parameters of the statistical model, which were estimated from the experimental data.

$\boldsymbol{\alpha}$	$\boldsymbol{\beta}$	$\boldsymbol{\delta}$
0.0712	14.6509	-31.5353

The combination of the stresses into the equivalent stress formulation is governed by four φ parameters in Table 8. It can be noted how the value of the coefficient to the stresses in fiber direction σ_1, φ_1, is smaller by an order of magnitude than the other terms. This ratio reflects that between the longitudinal and transverse stresses in the specimen and can be interpreted as a similar relative significance of both in the failure mechanism.

The cumulative distribution functions yielded by the calibrated model are plotted in Figure 39, one for each specimen width. An inverse size effect is evident from the curves. The critical equivalent stress in the wider specimens (w = 36 mm) for any given value of the probability of failure is lower than the one estimated for the narrower specimens (w = 24 mm).

An explanation for the size effect observed could be found in specimen geometry and material heterogeneity. The highest stresses generated around the hole are located in the tows in the longitudinal direction. The relative size of the tow to the hole decreases for an upscaled specimen, e.g. in a 36 mm wide compared to a 24 mm wide one. Because of the larger relative radius of the hole compared to tow size, the effective stress concentration factor for the tows around the hole is lowered. As a result, the distribution of stresses is improved in close vicinity to the hole, and the same material sees an increase in its load-bearing ability. An analogous effect takes place in the transverse tows. It is known that quasi-brittle behavior can be induced in brittle materials by introducing material heterogeneity [2]. In the present case, the UD carbon fiber reinforced composite constituting the tows has been made heterogeneous by weaving it into a twill fabric, and this effect is enhanced by considering larger (wider) specimens.

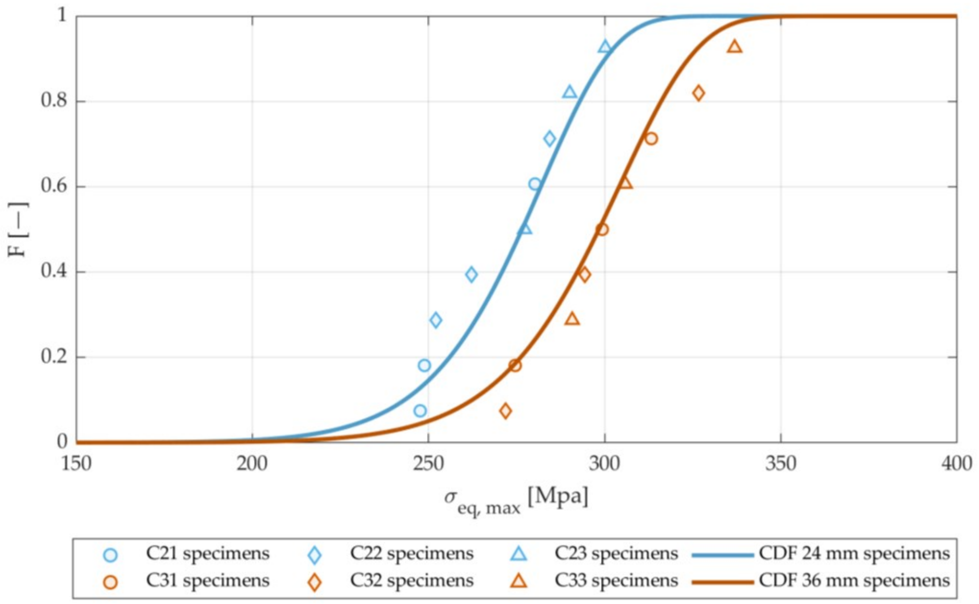

Figure 39. Plot of the model cumulative distribution, as a function of the maximum equivalent stress, for both the 24 mm and 36 mm specimen types. Markers are used to denote the experimental observation.

Different markers are used in the plot to indicate the various specimen width-to-diameter ratios. The approach taken considered only the specimen width as the prevalent scaling factor in the size effect. The observed distribution of the specimen hole diameters within each group validates this assumption, with the mixing of hole sizes along the curve suggesting a lower influence of width-to-diameter on size effect in the range of dimensions considered. This is most evident for the wider specimens. For instance, a specimen with the smallest notch diameter in its width group, C31, exhibits the third highest equivalent stress, while a specimen with the largest relative notch diameter, C33, has the third lowest equivalent stress.

Chapter 6

Final considerations

This chapter provides a summary of the results of this work. It includes Section 6.1, summarizing what has been achieved and the conclusions drawn, and Section 6.2, which discusses potential future research developments.

6.1 Conclusions

The objective of this work was to develop a statistical model to study the size effect on ultimate strength in open-hole woven composites. The methodology was successfully applied to a 2 × 2 twill CFRP composite, and scaling in width as well as width-to-diameter ratios were investigated. Conclusions will be drawn from the two main areas of this work: the mesoscale FEM modeling of the material from experimental data, and the statistical modeling using FEM stress data.

6.1.1 Mesoscale model

A 2D shell model that describes the material at mesoscale level was developed, in order to study the complex stress field from open-hole concentration in a twill weave composite material. Open-hole tensile tests were first conducted, measuring surface strain data with digital image correlation (DIC). A new semi-automated method using image processing techniques and DIC position data for mapping the material orientation at tow level was set up, and used to build FEM models representative of each individual tested specimen. This process subdivides the transversally isotropic fabric lamina in its orthotropic tows, with material orientation depending on the weave pattern. Tow-level material properties were obtained via a FEMU reverse identification process, by minimizing the error between the numerical and experimental-DIC strain.

The model proved effective in reproducing the complex stress and strain distributions in the twill weave composite material under open-hole tensile load, and it was validated against experimental test results. Since the proposed approach constructs the numerical model from an image of the actual specimen, captured directly on the tensile test fixture by the same camera apparatus used for DIC, the spatial correspondence of experimentally and numerically determined strain fields is inherently ensured. The numerical stress field provided by the model is dual in resolution and alignment with the experimental DIC strain field. This fact, in addition to the limited computational cost of the model, makes it particularly suitable for the implementation of reverse identification of material parameters and Finite Element Model Updating (FEMU) methods.

One downside of the model's simplicity is its inability to capture the undulation of the fiber tows resulting from to crimping in the textile, due to its simplified bidimensional nature. This translates in longitudinal elastic properties of the tows which are slightly lower than those of a pure unidirectional composite, as they are the average properties of the tow in the lamina plane.

A definite advantage of the proposed approach over traditional multiscale ones is the ability to conduct a mesoscale-level stress analysis without needing microscale-level material properties. This entirely avoids the complex preparation and testing of specimens of individual tows, fibers, or matrix. Instead, only standard coupon-level tests are performed, leveraging the spatial resolution of DIC rather than smaller-scale tests for enhanced detail.

6.1.2 Statistical model

Building on the stress data made available by the mesoscale modeling of the composite, a statistical model has been proposed that describes the mesoscale size effect on the strength of open-hole woven-reinforcement composites under tension.

The statistical model developed is based on discretizing the component into sub-volumes, each subjected to a uniform stress level. The sub-volumes are the elements of the mesoscale finite element model described in the previous section, with experimentally measured local orientation of the woven fiber reinforcement, and the stress in each element is computed from this model. To reduce dimensionality while still considering all stress components, an equivalent stress is defined at the material mesoscale level. This equivalent stress consists of four quadratic terms, similarly to the Tsai–Hill failure criterion. The random variable in the statistical model is the maximum equivalent stress in the component, whose probability is controlled by the scale effect. The statistical model, calibrated using experimental results of open-hole tensile tests, displayed significant accuracy in reproducing the mesoscopic scale effect that governs the failure of fiber tows.

A foundation of the proposed method is the mesoscale finite element model that considers both the interaction in the stress fields due to the material heterogeneity and the stress intensification caused by the notch. Only through a model with this level of detail it is possible to extract stress fields representative of the actual stress state in the component or specimen. Starting from the mesoscale stress field, the statistical model accurately predicts the empirical failure probability, achieving a 94% coefficient of determination. The model predicts a lower critical equivalent stress in wider specimens at a specified probability of failure.

Summarizing, the proposed method is an effective tool for predicting component strength while accounting for both the material heterogeneity and the scale effect that controls the failure of the carbon fiber tows constituting the woven composite.

6.2 Possible future developments

The research work presented here has the potential to lead to further developments. Three paths are suggested and briefly explored in this section.

1. While the simplicity of the mesoscale model is one of its main assets, some applications—especially at a scale smaller than the one considered—might require higher resolution. The model may be improved and made able to duplicate the undulation of tows in and out of the lamina plane by grading the elastic properties inside each fiber tow. Additional detail in the strain field may thus be provided without adding excessive complexity. The grading could follow a pre-defined function from existing laminate theory-based models of fabric weaves, such as [57]. Alternatively, an optimization technique similar to that developed in this work could be used, with DIC data and a numerical model, but operating on a single unit cell of the fabric.
2. The proposed methodology, while used in this work to study the size effect of circular notches, may potentially be applied to the stress analysis or statistical reliability study of any mechanical problem where considering mesoscale material heterogeneity in woven fiber composites is advantageous. Examples of similar applications are studying the effect of ply shift on open-hole stress concentration, the study of other shapes and locations of notches, the interaction of multiple notches, or different types of woven reinforcements, including hybrid ones. In particular, this same study could be extended into a comparative one by considering the same size effect in specimens with similar constituent fiber and matrix but different fabric weaves, such as plain weave or satin.

3. A possible development of the statistical model is the homogenization of the mesoscale model into a homogeneous, macroscale one, producing a readily usable design criterion for composite components with open-hole notches. Thus, starting with simple standardized tests on specimens of the same material used in designing composite parts, mesoscale-level information on reliability would be garnered through the experimental-numerical methodology developed here, and used to calibrate the reliability model. It would then be converted back into a macroscale reliability criterion to be used in mechanical design with conventional material modeling of composite material.

References

1. Wisnom, M.R. Size Effects in the Testing of Fibre-Composite Materials. *Compos Sci Technol* **1999**, *59*, 1937–1957, doi:10.1016/S0266-3538(99)00053-6.
2. Bazant, Z.P. Size Effect on Structural Strength: A Review. *Archive of Applied Mechanics* **1999**, *69*, 703–705.
3. Pagnoncelli, A.P.; Tridello, A.; Paolino, D.S. Modelling Size Effects for Static Strength of Brittle Materials. *Mater Des* **2020**, *195*, 109052, doi:10.1016/J.MATDES.2020.109052.
4. Green, B.G.; Wisnom, M.R.; Hallett, S.R. An Experimental Investigation into the Tensile Strength Scaling of Notched Composites. *Compos Part A Appl Sci Manuf* **2007**, *38*, 867–878, doi:10.1016/j.compositesa.2006.07.008.
5. Xu, X.; Wisnom, M.R.; Mahadik, Y.; Hallett, S.R. An Experimental Investigation into Size Effects in Quasi-Isotropic Carbon/Epoxy Laminates with Sharp and Blunt Notches. *Compos Sci Technol* **2014**, *100*, 220–227, doi:10.1016/j.compscitech.2014.06.002.
6. Pierron, F.; Green, B.G.; Wisnom, M.R. Full-Field Assessment of the Damage Process of Laminated Composite Open-Hole Tensile Specimens. Part I: Methodology. *Compos Part A Appl Sci Manuf* **2007**, *38*, 2307–2320, doi:10.1016/j.compositesa.2007.01.010.
7. Pierron, F.; Green, B.G.; Wisnom, M.R.; Hallett, S.R. Full-Field Assessment of the Damage Process of Laminated Composite Open-Hole Tensile Specimens. Part II: Experimental Results. *Compos Part A Appl Sci Manuf* **2007**, *38*, 2321–2332, doi:10.1016/j.compositesa.2007.01.019.
8. Qin, L.; Zhang, Z.; Feng, Z.; Li, X.; Wang, Y.; Wang, Y.; Miao, H.; He, L.; Gong, X. Full-Field Analysis of Notch Effects of 3D Carbon/Carbon Composites. *J Mater Sci* **2013**, *48*, 3454–3460, doi:10.1007/s10853-013-7135-x.
9. Awerbuch, J.; Madhukar, M.S. Notched Strength of Composite Laminates: Predictions and Experiments—A Review. *Journal of Reinforced Plastics and Composites* 1985, *4*, 3–159.

10. Green, B.G.; Wisnom, M.R.; Hallett, S.R. An Experimental Investigation into the Tensile Strength Scaling of Notched Composites. *Compos Part A Appl Sci Manuf* **2007**, *38*, 867–878, doi:10.1016/J.COMPOSITESA.2006.07.008.

11. Martin, E.; Leguillon, D.; Carrère, N. An Extension of the Point-Stress Criterion Based on a Coupled Stress and Energy Fulfilment: Application to the Prediction of the Open-Hole Tensile Strength of a Composite Plate. *Structural Integrity and Durability of Advanced Composites: Innovative Modelling Methods and Intelligent Design* **2015**, 425–444, doi:10.1016/B978-0-08-100137-0.00017-1.

12. Whitney, J.M.; Nuismer, R.J. Stress Fracture Criteria for Laminated Composites Containing Stress Concentrations. *J Compos Mater* **1974**, *8*, 253–265, doi:10.1177/002199837400800303.

13. Batista, A.C.M.C.; Tinô, S.R.L.; Fontes, R.S.; Nóbrega, S.H.S.; De Aquino, E.M.F. Analytical, Experimental and Finite Element Analysis of the Width/Diameter Hole Ratio Effect in Vinylester/Carbon Hybrid Twill Weave Composites. *Composites Part C: Open Access* **2020**, *2*, 100033, doi:10.1016/j.jcomc.2020.100033.

14. Tinô, S.R.L.; Fontes, R.S.; De Aquino, E.M.F. Theories of Failure Average Stress Criterion and Point Stress Criterion in Notched Fiber-Reinforced Plastic. *J Compos Mater* **2014**, *48*, 2669–2676, doi:10.1177/0021998313501920.

15. Fontes, R.S.; Bezerra, H.A.D.; De Caldas Batista, A.C.M.; Tinô, S.R.L.; De Aquino, E.M.F. Failure Theories and Notch Type Effects on the Mechanical Properties of Jute-Glass Hybrid Composite Laminates. *Materials Research* **2019**, *22*, e20180269, doi:10.1590/1980-5373-MR-2018-0269.

16. Khechai, A.; Tati, A.; Guerira, B.; Guettala, A.; Mohite, P.M. Strength Degradation and Stress Analysis of Composite Plates with Circular, Square and Rectangular Notches Using Digital Image Correlation. *Compos Struct* **2018**, *185*, 699–715, doi:10.1016/J.COMPSTRUCT.2017.11.060.

17. Sattar, S.; Pedrazzoli, D.; Zhang, M.; Kravchenko, S.G.; Kravchenko, O.G. Notched Tensile Strength of Long Discontinuous Glass Fiber Reinforced Nylon Composite. *Compos Part A Appl Sci Manuf* **2022**, *163*, 107217, doi:10.1016/j.compositesa.2022.107217.

18. Serra, J.; Bouvet, C.; Karinja Haridas, P.; Ratsifandrihana, L. Numerical Simulations of Combined Size Effects Acting on an Open-Hole Laminated Composite Plate under Tension. *J Compos Mater* **2023**, *57*, 213–233, doi:10.1177/00219983221139791.

19. Hallett, S.R.; Green, B.G.; Jiang, W.G.; Wisnom, M.R. An Experimental and Numerical Investigation into the Damage Mechanisms in Notched Composites. *Compos Part A Appl Sci Manuf* **2009**, *40*, 613–624, doi:10.1016/j.compositesa.2009.02.021.

20. Camanho, P.P.; Maimí, P.; Dávila, C.G. Prediction of Size Effects in Notched Laminates Using Continuum Damage Mechanics. *Compos Sci Technol* **2007**, *67*, 2715–2727, doi:10.1016/j.compscitech.2007.02.005.

21. Camanho, P.P.; Erçin, G.H.; Catalanotti, G.; Mahdi, S.; Linde, P. A Finite Fracture Mechanics Model for the Prediction of the Open-Hole Strength of Composite Laminates. *Compos Part A Appl Sci Manuf* **2012**, *43*, 1219–1225, doi:10.1016/j.compositesa.2012.03.004.

22. Chen, B.Y.; Tay, T.E.; Baiz, P.M.; Pinho, S.T. Numerical Analysis of Size Effects on Open-Hole Tensile Composite Laminates. *Compos Part A Appl Sci Manuf* **2013**, *47*, 52–62, doi:10.1016/j.compositesa.2012.12.001.

23. Serra, J.; Bouvet, C.; Castanié, B.; Petiot, C. Scaling Effect in Notched Composites: The Discrete Ply Model Approach. *Compos Struct* **2016**, *148*, 127–143, doi:10.1016/j.compstruct.2016.03.062.

24. Serra, J.; Bouvet, C.; Castanié, B.; Petiot, C. Experimental and Numerical Analysis of Carbon Fiber Reinforced Polymer Notched Coupons under Tensile Loading. *Compos Struct* **2017**, *181*, 145–157, doi:10.1016/j.compstruct.2017.08.090.

25. Zheng, K.; Hu, H.; Cao, D.; Zhong, Y.; Li, S. Experimental and Numerical Studies on the Tensile Behaviors of Thin-Ply and Thick-Ply Open-Hole Laminates. *Thin-Walled Structures* **2023**, *186*, 110649, doi:10.1016/j.tws.2023.110649.

26. Yu, J.; Pan, Z.; Cai, Q.; Zhang, F.; Wu, Z. Open Hole Tensile Behavior of Plain Woven Carbon/Glass Hybrid Composites. *Int J Mech Sci* **2023**, *246*, 108142, doi:10.1016/j.ijmecsci.2023.108142.

27. Wysmulski, P. Failure Mechanism of Tensile CFRP Composite Plates with Variable Hole Diameter. *Materials* **2023**, *16*, 4714, doi:10.3390/ma16134714.

28. Ma, Z.; Chen, J.; Yang, Q.; Li, Z.; Su, X. Progressive Fracture Analysis of the Open-Hole Composite Laminates: Experiment and Simulation. *Compos Struct* **2021**, *262*, 113628, doi:10.1016/j.compstruct.2021.113628.

29. Swindeman, M.J.; Iarve, E. V.; Brockman, R.A.; Mollenhauer, D.H.; Hallett, S.R. Strength Prediction in Open Hole Composite Laminates by Using

Discrete Damage Modeling. *AIAA Journal* **2013**, *51*, 936–945, doi:10.2514/1.J051773.

30. Jočić, E.; Marjanović, M. Progressive Failure Analysis of Open-Hole Composite Laminates Using FLWT-SCB Prediction Model. *Int J Mech Sci* **2022**, *227*, 107407, doi:10.1016/j.ijmecsci.2022.107407.
31. Erçin, G.H.; Camanho, P.P.; Xavier, J.; Catalanotti, G.; Mahdi, S.; Linde, P. Size Effects on the Tensile and Compressive Failure of Notched Composite Laminates. *Compos Struct* **2013**, *96*, 736–744, doi:10.1016/j.compstruct.2012.10.004.
32. Nguyen-Hoang, M.; Becker, W. Open Holes in Composite Laminates with Finite Dimensions: Structural Assessment by Analytical Methods. *Archive of Applied Mechanics* **2022**, *92*, 1101–1125, doi:10.1007/s00419-021-02095-w.
33. Anzelotti, G.; Nicoletto, G.; Riva, E. Mesomechanic Strain Analysis of Twill-Weave Composite Lamina under Unidirectional in-Plane Tension. *Compos Part A Appl Sci Manuf* **2008**, *39*, 1294–1301, doi:10.1016/j.compositesa.2008.01.006.
34. Schreier, H.; Orteu, J.J.; Sutton, M.A. *Image Correlation for Shape, Motion and Deformation Measurements: Basic Concepts, Theory and Applications*; Springer US, 2009; ISBN 9780387787466.
35. Bruno, L. Mechanical Characterization of Composite Materials by Optical Techniques: A Review. *Opt Lasers Eng* **2018**, *104*, 192–203, doi:10.1016/j.optlaseng.2017.06.016.
36. Hild, F.; Roux, S. Digital Image Correlation: From Displacement Measurement to Identification of Elastic Properties – a Review. *Strain* **2006**, *42*, 69–80, doi:10.1111/J.1475-1305.2006.00258.X.
37. Caminero, M.A.; Lopez-Pedrosa, M.; Pinna, C.; Soutis, C. Damage Monitoring and Analysis of Composite Laminates with an Open Hole and Adhesively Bonded Repairs Using Digital Image Correlation. *Compos B Eng* **2013**, *53*, 76–91, doi:10.1016/j.compositesb.2013.04.050.
38. Lanza Di Scalea, F.; Hong, S.S.; Cloud, G.L. Whole-Field Strain Measurement in a Pin-Loaded Plate by Electronic Speckle Pattern Interferometry and the Finite Element Method. *Exp Mech* **1998**, *38*, 55–60, doi:10.1007/BF02321268/METRICS.
39. Réthoré, J.; Muhibullah; Elguedj, T.; Coret, M.; Chaudet, P.; Combescure, A. Robust Identification of Elasto-Plastic Constitutive Law Parameters from

Digital Images Using 3D Kinematics. *Int J Solids Struct* **2013**, *50*, 73–85, doi:10.1016/J.IJSOLSTR.2012.09.002.

40. Réthoré, J. A Fully Integrated Noise Robust Strategy for the Identification of Constitutive Laws from Digital Images. *Int J Numer Methods Eng* **2010**, *84*, 631–660, doi:10.1002/NME.2908.
41. He, T.; Liu, L.; Makeev, A. Uncertainty Analysis in Composite Material Properties Characterization Using Digital Image Correlation and Finite Element Model Updating. *Compos Struct* **2018**, *184*, 337–351, doi:10.1016/J.COMPSTRUCT.2017.10.009.
42. Tabiei, A.; Sun, J. Statistical Aspects of Strength Size Effect of Laminated Composite Materials. *Compos Struct* **1999**, *46*, 209–216, doi:10.1016/S0263-8223(99)00056-2.
43. Behera, A.; Thawre, M.M.; Ballal, A. Failure Analysis of CFRP Multidirectional Laminates Using the Probabilistic Weibull Distribution Model under Static Loading. *Fibers and Polymers* **2019**, *20*, 2390–2399, doi:10.1007/s12221-019-1194-9.
44. Khashaba, U.A.; Sebaey, T.A.; Alnefaie, K.A. Failure and Reliability Analysis of Pinned-Joints Composite Laminates: Effects of Stacking Sequences. *Compos B Eng* **2013**, *45*, 1694–1703, doi:10.1016/j.compositesb.2012.09.066.
45. Kumar Singh, K.; Shanmugam, R.; Touhid Alam Ansari, M.; Gaurav, A. Reliability Analysis of Angle Ply Woven GFRP Composite under In-Plane Loading Condition Using Two Parameter Weibull Distribution. *Mater Today Proc* **2023**, doi:10.1016/j.matpr.2023.05.164.
46. Marston, C.; Gabbitas, B.; Adams, J.; Nutt, S.; Marshall, P.; Galiotis, C. Failure Characteristics in Carbon/Epoxy Composite Tows. *Compos Part A Appl Sci Manuf* **1996**, *27*, 1183–1194, doi:10.1016/1359-835X(96)00076-0.
47. Mesquita, F.; Breite, C.; Lomov, S. V.; Swolfs, Y. In-Situ Synchrotron Computed Tomography Tensile Testing of Composite Specimens to Estimate Fibre Strength Weibull Parameters. *Compos Sci Technol* **2022**, *229*, 109710, doi:10.1016/j.compscitech.2022.109710.
48. Pimenta, S.; Pinho, S.T. Hierarchical Scaling Law for the Strength of Composite Fibre Bundles. *J Mech Phys Solids* **2013**, *61*, 1337–1356, doi:10.1016/J.JMPS.2013.02.004.
49. Paolino, D.S. Very High Cycle Fatigue Life and Critical Defect Size: Modeling of Statistical Size Effects. *Fatigue Fract Eng Mater Struct* **2021**, *44*, 1209–1224, doi:10.1111/FFE.13424.

50. Invernizzi, S.; Paolino, D.; Montagnoli, F.; Tridello, A.; Carpinteri, A. Comparison between Fractal and Statistical Approaches to Model Size Effects in VHCF. *Metals 2022, Vol. 12, Page 1499* **2022**, *12*, 1499, doi:10.3390/MET12091499.

51. Bacarreza, O.; Wen, P.; Aliabadi, M.H. Micromechanical Modelling of Textile Composites. In *Computational and Experimental Methods in Structures: Volume 6—Woven Composites*; Aliabadi, M.H., Ed.; World Scientific Publishing Co. Pte Ltd, 2015; Vol. 6, pp. 1–74 ISBN 9781493990047.

52. Bacarreza, O.; Wen, P.; Aliabadi, M.H. Micromechanical Modelling of Textile Composites. *Computational and Experimental Methods in Structures* **2015**, *6*, 1–74, doi:10.1142/9781783266180_0001.

53. Ishikawa, T.; Chou, T.W. Stiffness and Strength Behaviour of Woven Fabric Composites. *J Mater Sci* **1982**, *17*, 3211–3220, doi:10.1007/BF01203485.

54. Naik, N.K.; Ganesh, V.K. Prediction of On-Axes Elastic Properties of Plain Weave Fabric Composites. *Compos Sci Technol* **1992**, *45*, 135–152, doi:10.1016/0266-3538(92)90036-3.

55. Shembekar, P.S.; Naik, N.K. Elastic Behavior of Woven Fabric Composites: II—Laminate Analysis. *http://dx.doi.org/10.1177/002199839202601503* **1992**, *26*, 2226–2246, doi:10.1177/002199839202601503.

56. Naik, N.K.; Shembekar, P.S. Elastic Behavior of Woven Fabric Composites: III—Laminate Design. *http://dx.doi.org/10.1177/002199839202601704* **1992**, *26*, 2522–2541, doi:10.1177/002199839202601704.

57. Chaphalkar, P.; Kelkar, A.D. Classical Laminate Theory Model for Twill Weave Fabric Composites. *Compos Part A Appl Sci Manuf* **2001**, *32*, 1281–1289, doi:10.1016/S1359-835X(01)00101-4.

58. Kwon, Y.W.; Roach, K. Unit-Cell Model of 2/2-Twill Woven Fabric Composites for Multi-Scale Analysis. *CMES - Computer Modeling in Engineering and Sciences* **2004**, *5*, 63–72.

59. Goyal, D.; Tang, X.; Whitcomb, J.D.; Kelkar, A.D. Effect of Various Parameters on Effective Engineering Properties of 2 × 2 Braided Composites. *Mechanics of Advanced Materials and Structures* **2005**, *12*, 113–128, doi:10.1080/15376490490493998.

60. Nicoletto, G.; Riva, E. Failure Mechanisms in Twill-Weave Laminates: FEM Predictions vs. Experiments. *Compos Part A Appl Sci Manuf* **2004**, *35*, 787–795, doi:10.1016/j.compositesa.2004.01.007.

61. Ng, S.P.; Tse, P.C.; Lau, K.J. Progressive Failure Analysis of 2/2 Twill Weave Fabric Composites with Moulded-in Circular Hole. *Compos B Eng* **2001**, *32*, 139–152, doi:10.1016/S1359-8368(00)00040-8.

62. ASTM International D5766—Standard Test Method for Open-Hole Tensile Strength of Polymer Matrix Composite Laminates. *Annual Book of ASTM Standards* **2011**, 1–8, doi:10.1520/D5766.

63. ASTM International D3039—Standard Test Method for Tensile Properties of Polymer Matrix Composite Materials. *Annual Book of ASTM Standards* **2014**, 1–13, doi:10.1520/D3039.

64. ASTM International D3518—Standard Test Method for in-Plane Shear Response of Polymer Matrix Composite Materials by Tensile Test of a ±45° Laminate. *Annual Book of ASTM Standards* **2018**, 1–8, doi:10.1520/D3518.

65. Le Louët, V.; Rousseau, B.; Le Corre, S.; Boyard, N.; Tardif, X.; Delmas, J.; Delaunay, D. Study of the Reflective Behaviour of Carbon Fibres Reinforced Polymer Composite up to 450°C. *AIP Conf Proc* **2017**, *1896*, doi:10.1063/1.5008149.

66. Zou, Y.; Zhang, L.; Zhang, J.; Li, B.; Lv, X. Developmental Trends in the Application and Measurement of the Bidirectional Reflection Distribution Function. *Sensors 2022, Vol. 22, Page 1739* **2022**, *22*, 1739, doi:10.3390/S22051739.

67. Lloyd, S.P. Least Squares Quantization in PCM. *IEEE Trans Inf Theory* **1982**, *28*, 129–137, doi:10.1109/TIT.1982.1056489.

68. Livermore Software Technology Corporation *LS-DYNA R12 Keyword User's Manual Volume II: Material Models*; 2020; Vol. II; ISBN 0977854035.

69. Gutmann, H.M. A Radial Basis Function Method for Global Optimization. *Journal of Global Optimization* **2001**, *19*, 201–227, doi:10.1023/A:1011255519438/METRICS.

70. PyPI Lasso-Python 2.0.3 Available online: https://pypi.org/project/lasso-python/.

71. Benard, A.; Bos-Levenbach, E.C. Het Uitzetten van Waarnemingen Op Waarschijnlijkdeids-Papier (The Plotting of Observations on Probability Paper). *Stat Neerl* **1953**, *7*, 163–173, doi:10.1111/J.1467-9574.1953.TB00821.X.

72. Nelder, J.A.; Mead, R. A Simplex Method for Function Minimization. *Comput J* **1965**, *7*, 308–313, doi:10.1093/comjnl/7.4.308.